

## Thermodynamic Retrieval in Rapidly Rotating Vortices from Multiple-Doppler Radar Data

ANNETTE M. FOERSTER

*Department of Atmospheric Sciences, University of Hawai'i at Mānoa, Honolulu, Hawaii*

MICHAEL M. BELL

*Department of Atmospheric Science, Colorado State University, Fort Collins, Colorado*

(Manuscript received 14 April 2017, in final form 7 August 2017)

### ABSTRACT

Thermodynamic retrievals can derive pressure and temperature information from kinematic measurements in regions where no in situ observations are available. This study presents a new retrieval technique called SAMURAI-TR (Spline Analysis at Mesoscale Utilizing Radar and Aircraft Instrumentation–Thermodynamic Retrieval) that derives three-dimensional fields of pressure and density potential temperature from multiple-Doppler radar data using a variational approach. SAMURAI-TR advances existing methods by 1) allowing for a horizontal variation in the reference-state definition and 2) representing the retrieved quantities of pressure and temperature as three-dimensional functions consisting of a series of finite-element cubic B-splines. The first advancement enables the retrieval to explicitly account for the large radial gradient of the mean thermodynamic state in tropical cyclones and other rapidly rotating vortices. The second advancement allows for specification of the three-dimensional pressure and temperature gradients as pseudo-observations from Doppler-derived winds, effectively linking the vertical levels without the use of the thermodynamic equation or a microphysical closure. The retrieval uses only the horizontal and vertical momentum equations, their derivatives, and low-pass filters. The accuracy and sensitivity of the retrieval are assessed using a WRF simulation of a tropical cyclone. SAMURAI-TR has good accuracy compared to prior techniques and retrieves pressure to within 0.25 hPa and temperature to within 0.7 K RMSE. The application of the method to real data is demonstrated using multiple-Doppler data from Hurricane Rita (2005).

### 1. Introduction

High-resolution three-dimensional thermodynamic fields are highly desired observations in mesoscale weather systems, but they are some of the most difficult to obtain. Direct in situ measurements of pressure and temperature above the surface are limited to the paths of aircraft, radiosondes, and dropsondes, and it is unfeasible to completely sample the three-dimensional space in a weather system with these platforms. Remote sensing from spaceborne microwave radiometers can provide three-dimensional thermodynamic fields in precipitation through inversions of hyperspectral imagery but only at coarse spatial resolution. Because of these deficiencies in our observing capability, thermodynamic retrieval techniques using multiple-Doppler radar–derived winds have been developed to help

improve our understanding of mesoscale weather. In this study, we develop a new retrieval technique that can be applied to rapidly rotating vortices such as tropical cyclones (TCs) with good numerical accuracy.

Seminal work by Gal-Chen (1978) described the basic approach of using the horizontal and vertical momentum equations to infer thermodynamic properties from kinematic measurements made by Doppler radars. Gal-Chen developed a Poisson equation to solve for the pressure field at a constant altitude given a known horizontal wind field with random errors. Neumann boundary conditions for this solution could be imposed directly from the radar winds at the irregular boundary of available radar scatterers, making this technique an attractive method for deducing the pressure field inside isolated mesoscale convective systems (MCSs) such as supercells or squall lines. The perturbation density and temperature fields could then be obtained using the vertical momentum equation. A fundamental limitation of this pioneering technique was the presence of an

Corresponding author: Annette M. Foerster, foerster@hawaii.edu

unresolved integration constant at each vertical level, making fully three-dimensional thermodynamic fields reliant on at least one external absolute measurement of pressure and temperature at each vertical level within the domain to couple the vertical levels. Gal-Chen briefly described an alternate technique for obtaining the density through cross differentiation of the horizontal momentum equations in his appendix A, but this was not implemented in that study and the problem of coupling the vertical levels remained.

Roux (1985) advanced the technique in several key ways. By using an alternate form of the momentum equations with potential temperature and nondimensional pressure as the retrieved variables, and implementing the cross differentiation originally proposed by Gal-Chen (1978), Roux was able to add a simplified form of the thermodynamic equation as an additional constraint in a variational cost function. The vertical levels could be effectively coupled through a microphysical closure that roughly closed the thermodynamic budget under a steady-state assumption, neglecting ice phase changes. This technique was further refined to improve the microphysical closure and numerical stability, yielding an effective three-dimensional thermodynamic retrieval that required only a single integration constant for the entire domain (Roux 1988; Roux and Ju 1990; Roux et al. 1993).

Protat et al. (1998) improved the technique by retrieving the thermodynamic fields analytically. In contrast to the gridpoint representation used in the techniques of Gal-Chen and Roux, the input and output fields were represented by orthonormal functions, for example, fifth-order Legendre polynomials. This allowed for natural interpolation and natural filtering, direct integration and differentiation without spatial discretization, and an analytic representation of the variables and their spatial derivatives. The technique showed skill at various scales of motion, in particular at mesoscale (Lemaitre et al. 1999; Protat and Lemaitre 2001). Similar to Gal-Chen's approach, this method relies on *in situ* measurements to determine the unresolved integration constant at each vertical level in order to couple the vertical levels. In absence of these external measurements of pressure and temperature, the interpretation of the retrieval results is limited to the horizontal gradients of the thermodynamic fields (Protat and Lemaitre 2001).

Liou (2001) and Liou et al. (2003) further improved the thermodynamic retrieval technique by using a different variational form that was able to avoid both the microphysical closure and cross differentiation of the horizontal momentum equations by treating the heat source/sink as a retrieved variable. This technique

successfully demonstrated that a fully three-dimensional solution could be obtained with good numerical accuracy by including the thermodynamic equation and penalty constraints for low-pass filtering in a single variational cost function, in contrast to previous formulations that used separate cost functions for pressure and temperature. Further modifications to the cost function formulation and the addition of a convective adjustment scheme described in Liou et al. (2014) show that this technique is a viable method for initializing convective-scale numerical weather prediction models as originally envisioned by Gal-Chen (1978).

While the specific formulations used to retrieve the thermodynamic fields have continued to improve over the past few decades and have added additional constraints, such as the vorticity equation (Protat and Zawadzki 2000; Liou and Chang 2009), all of these previous techniques share the common element that thermodynamic perturbations are solved relative to a hydrostatic base state that varies only in the vertical. The assumption that the perturbations are small relative to the base state is generally well supported in MCSs, where the weather system can be approximately regarded as distinct from the ambient, quiescent environment, and the neglect of nonlinear quadratic perturbation terms in the cost function is justified. However, as the perturbations become large with respect to the environment, such as the case of a warm-cored TC, the pressure and temperature gradients can become quite steep and the separation of the "mean" from the "perturbation" becomes problematic. Since the physical interpretation of the buoyancy and perturbation pressure gradients as forcing terms for vertical motion is also dependent on the base state chosen for the retrieval, the use of a horizontally homogeneous reference state becomes both numerically and conceptually difficult.

Doswell and Markowski (2004) provided a thorough discussion of the definition of buoyancy and demonstrated that weather systems cannot know anything about the relative thermodynamic quantities of nearby air parcels as defined by an arbitrary reference state in a numerical weather prediction (NWP) model, but rather respond to the combined forcing from the total temperature and pressure gradients at each grid point. The reference state can be chosen somewhat arbitrarily in an NWP model, since the full thermodynamic fields are known, but with observations we can retrieve only the perturbations relative to our defined reference state (and in some cases a domainwide constant). Choosing a relevant reference state therefore both improves the numerical accuracy of the retrieval and makes the physical interpretation of the resulting perturbations more meaningful.

Studies on the importance of the buoyancy force on convection in the TC eyewall (Zhang et al. 2000; Braun 2002; Eastin et al. 2005) have shown seemingly contradictory results, partly because of different reference-state definitions. Smith et al. (2005) argued that the axisymmetric vortex in thermal wind balance was the most appropriate base state for a rapidly rotating vortex given an approximate force balance in both the horizontal and vertical. For example, the inner-core region of a TC features a prominent radial pressure drop and temperature increase toward the center of the system. This pressure drop and temperature increase are largely balanced by the centrifugal and Coriolis forces associated with the primary (swirling) circulation, and thus a large fraction of the pressure and temperature gradients do not contribute to forcing or altering the secondary (vertical and radial) circulation. Smith et al. (2005) derived a generalized buoyancy force for vortices that is relative to the sloping isobaric surfaces in gradient wind balance. In the current study, we apply this concept to the thermodynamic retrieval of rapidly rotating vortices in conjunction with an improved numerical formulation.

While the primary application in most previous thermodynamic retrievals has been to MCSs, some estimates of the bulk thermodynamic fields have been obtained in strong vortices. The method of Roux et al. (1993) was modified for cylindrical coordinates by Viltard and Roux (1998) using a single-Doppler wind retrieval to estimate the low azimuthal wavenumber pressure and temperature field of Hurricane Claudette (1991), which consisted largely of the axisymmetric pressure drop and warm core found to be approximately in thermal wind balance. An axisymmetric retrieval of pressure in the Mulhall tornado using the gradient wind equation and pressure advection terms from a single-Doppler wind retrieval was performed by Lee and Wurman (2005), revealing a similar morphological structure to that found in a TC with a large central pressure drop and sloping isobaric surfaces. Retrievals of the detailed thermodynamic structure have also been conducted using time-dependent data assimilation including 4DVAR (Tai et al. 2017) and ensemble Kalman filter techniques (Marquis et al. 2014). While time-dependent data assimilation techniques show great promise, they rely on a different set of assumptions, model physics, and error sources than the classical techniques that directly retrieve thermodynamics from the observations and are not considered further here. To the authors' knowledge, detailed three-dimensional pressure and temperature fields in a TC or tornado derived solely from observations have not been reported in the literature.

The new thermodynamic retrieval technique presented here provides several advances over existing methods. One primary advance is the reformulation of

the retrieval equations to allow for horizontal variation in the balanced reference state. This innovation allows for a two-step retrieval process in which the dominant balanced thermal fields are calculated first, followed by a detailed retrieval of perturbations relative to that horizontally varying balanced state (i.e., vortex-scale pressure deficit and warm core). The two-step retrieval minimizes the unresolved integration constant at each level as a result of physical constraints on the departures from balance, and it does not require in situ measurements within the retrieval domain.

The second significant advance is the use of a finite-element approach in the numerical formulation of the variational cost function. Instead of a traditional grid-point representation of the three-dimensional fields, the pressure and temperature are represented as functions consisting of a series of overlapping cubic B-splines (Ooyama 1987, 2002). The finite-element representation yields a scale-controlled analysis with efficient low-pass filtering and analytic spatial derivatives (Bell et al. 2012). This approach allows for the specification of pseudo-observations of the pressure gradient from the multi-Doppler winds that are implicitly integrated during the cost function minimization. The natural filtering capabilities of the finite-element representation are similar to those of an analytic representation with Legendre polynomials. In addition, the spline analysis effectively couples the vertical levels without the use of the thermodynamic equation or a microphysical closure. The method does require the cross differentiation of the horizontal momentum equations, but it does not require additional physical constraints.

The outline of the paper is as follows. Section 2 describes the details of the new thermodynamic retrieval method for rapidly rotating vortices. Section 3 presents an evaluation of the retrieval using a Weather Research and Forecasting (WRF) Model simulation of Hurricane Rita (2005). The errors in the temperature and pressure retrievals are quantified by assessing the retrieval performance at different storm intensities compared to the reference WRF Model fields, and sensitivity studies are conducted. Section 4 demonstrates the applicability of the thermodynamic retrieval using real data of Hurricane Rita (2005) collected during the Hurricane Rainband and Intensity Change Experiment (RAINEX) field campaign (Houze et al. 2006). Section 5 summarizes and discusses the results.

## 2. Method

The retrieval of the temperature and pressure perturbations from Doppler radar data is performed in three distinct steps. First, the radar data (and optionally

other observational data) are combined into a three-dimensional analysis of wind and precipitation fields using the software tool called Spline Analysis at Mesoscale Utilizing Radar and Aircraft Instrumentation (SAMURAI; [Bell et al. \(2012\)](#)). Second, the balanced reference-state temperature and pressure fields are calculated to facilitate the retrieval and the interpretation of the perturbations. Third, the temperature and pressure perturbations are retrieved by variationally solving a set of modified momentum equations with SAMURAI-Thermodynamic Retrieval (SAMURAI-TR). Details of each of the three steps are described in the following subsections.

#### *a. Wind retrieval*

The SAMURAI software estimates the most likely state of the atmosphere based on observations. It can combine different types of observations, such as radar data, in situ dropsonde and flight level data, satellite atmospheric motion vectors, and other data types, specifying the error characteristics individually for each type of observation. It is possible to incorporate model fields from global or mesoscale models as background estimates and to add balance or physical constraints, such as mass continuity. SAMURAI solves for the most likely atmospheric state by minimizing a cost function in incremental form  $J(\hat{\mathbf{x}})$  that avoids the inversion of the background error covariance matrix by using a control variable  $\hat{\mathbf{x}}$ :

$$J(\hat{\mathbf{x}}) = \frac{1}{2} \hat{\mathbf{x}}^T \hat{\mathbf{x}} + \frac{1}{2} (\mathbf{H} \mathbf{C} \hat{\mathbf{x}} - d)^T \mathbf{R}^{-1} (\mathbf{H} \mathbf{C} \hat{\mathbf{x}} - d), \quad (1)$$

where  $\mathbf{H}$  denotes the linearized observation operator,  $\mathbf{C}$  denotes the square root of the background error covariance matrix,  $\mathbf{R}$  denotes the observation error covariance matrix, and  $d \equiv \mathbf{y} - h(\mathbf{x}_b)$  denotes the difference between the observations  $\mathbf{y}$  and the nonlinear observation operator applied to the background state estimate  $h(\mathbf{x}_b)$ . For linear operators such as radial velocity or in situ measurements  $h$  and  $\mathbf{H}$  are equivalent. The background errors can be set individually for each type of observation and each type of background. For more details on the variational cost function, see [Gao et al. \(2004\)](#). The cost function is minimized using a conjugate gradient algorithm, including a cubic spline transform and low-pass filter operations as part of the  $\mathbf{C}$  operator. SAMURAI solves for the control variable  $\mathbf{x} = \{\rho_u, \rho_v, \rho_w, T', q'_v, \rho'_a\}$ , where  $\rho_u$ ,  $\rho_v$ , and  $\rho_w$  are the moist-air-density-weighted wind components,  $T$  denotes temperature,  $q'_v$  denotes the water vapor mixing ratio, and  $\rho'_a$  denotes dry-air density. The primes denote thermodynamic perturbations defined

relative to a horizontally homogeneous hydrostatic environmental reference state. The hydrostatic reference state is used in the wind retrieval as a numerical expedient to avoid solving for the strong vertical gradients in thermodynamic quantities, and as a reference density profile for mass continuity. In this study the [Dunion \(2011\)](#) moist tropical sounding was used as the environmental reference profile. Pressure perturbations are derived from the temperature and density perturbations via the ideal gas law. The SAMURAI output then contains the analyzed control variables and the spatial derivatives of the wind field and other derived quantities.

The use of the spline basis for the underlying representation of the atmospheric structure provides several benefits over a gridpoint representation. In this approach the analyzed structure is represented by a series of nodal coefficients that determine the amplitude of overlapping cubic B-spline finite elements. Since the basis functions are analytic, one can directly specify “pseudo-observations” of spatial gradients that are implicitly integrated during the cost function minimization. Through this technique, mass continuity is enforced by specifying pseudo-observations of the momentum gradients at the spline nodes, avoiding explicit integration of the mass continuity equation.

Note that the estimate of the thermodynamic state of the atmosphere is usually based on very limited in situ observations that are not sufficient to construct a full 3D field. Extensive in situ sampling or a background estimate can mitigate this shortcoming to some extent. The accuracy of the wind field is highly dependent on the radar sampling geometry. In the case of a well-resolved geometry without Doppler errors, the accuracy of the wind field is estimated to be less than  $2 \text{ m s}^{-1}$  ([Hildebrand et al. 1996](#)). SAMURAI has three spatial filters that can be used both to smooth the analysis and to spread information from the observations throughout the domain. The first filter, a Fourier spectral filter, allows for elimination of high-wavenumber features in the spectral domain. The second filter, the “spline cutoff,” operates on the finite-element basis during the spline transform and is described in detail by [Ooyama \(2002\)](#). It is implemented as a third derivative constraint on the cubic B-spline representation of the analysis. The third filter, a Gaussian recursive filter, is described in detail by [Purser et al. \(2003\)](#). This filter models a Gaussian low-pass filter through an efficient recursive operator. The filters can be used individually or can be combined to produce different spectral responses. For this study, a combination of the spline-cutoff filter and the Gaussian recursive filter was used, with the filter wavelengths set to 10 nodal points and 4 nodal points, respectively.

Interested readers are referred to [Bell et al. \(2012\)](#) and [Foerster et al. \(2014\)](#) for additional technical details about SAMURAI.

### b. Thermal-wind-balanced reference state

The vertical momentum equation states that the vertical acceleration is caused by the sum of the pressure gradient force and the gravitational force, which can be rewritten in terms of buoyancy and vertical perturbation pressure gradient force:

$$\frac{Dw}{Dt} = -\frac{1}{\rho} \frac{\partial p}{\partial z} - g = -\frac{1}{\rho} \frac{\partial p'}{\partial z} + b, \quad (2)$$

where  $w$  is the vertical velocity,  $D/Dt$  is the material derivative,  $t$  is the time,  $p$  is the pressure, and  $z$  is the height. The vertical acceleration  $Dw/Dt$  is uniquely defined, but the partitioning into buoyancy and the vertical perturbation pressure gradient depends on the definition of the perturbation and reference states.

This ambiguity of the buoyancy definition can make the interpretation of vertical forces challenging and emphasizes the importance of an appropriate reference-state definition. For ordinary tropical convection, the horizontal mean is a good choice because the horizontal changes in environmental temperature and pressure are small. For rapidly rotating vortices, however, the pressure and temperature surfaces slope significantly with radius, suggesting the use of the mean vortex in thermal wind balance as the reference state as proposed by [Smith et al. \(2005\)](#). This thermal-wind-balanced reference state can be calculated without approximation from the azimuthally averaged tangential wind field and the vertical temperature and pressure profiles at large radius ([Smith 2006](#)). Smith showed that combining the vertical and radial derivatives of the gradient wind and hydrostatic balance relationships, respectively, gives a linear first-order partial differential equation for thermal wind balance that can be solved using the method of characteristics. The characteristics are the surfaces of constant pressure:

$$\frac{dz}{dr} = \frac{1}{g} \left( \frac{\bar{V}_T^2}{r} + f \bar{V}_T \right). \quad (3)$$

The variation in density potential temperature along these characteristics is

$$\frac{\partial \ln \bar{\theta}_p}{\partial r} = \frac{1}{g} \frac{\partial}{\partial z} \left( \frac{\bar{V}_T^2}{r} + f \bar{V}_T \right), \quad (4)$$

where  $\bar{V}_T$  is the azimuthally averaged tangential wind,  $r$  is the radius,  $z$  is the altitude,  $f$  is the Coriolis

parameter,  $g$  is the gravitational acceleration, and  $\bar{\theta}_p$  is the azimuthally averaged density potential temperature, which includes the contribution of condensate loading to density. Density potential temperature is defined as  $\bar{\theta}_p = T_p (p_0/p)^{R_d/c_p}$ , where the density temperature  $T_p = p/(\rho R_d)$  includes contributions of dry air and water in its various states via the total density  $\rho = \rho_a + \rho_m + \rho_r$ , with subscripts  $a, m, r$  representing dry air, nonprecipitating moisture (including vapor and condensate), and precipitation (including rain and ice), respectively.

Equations (3) and (4) can be used to calculate the temperature and pressure fields of the balanced state by integrating the thermal wind equation inward from the outer boundaries, where the boundary conditions are given by vertical temperature and pressure profiles. The SAMURAI analysis obtained in the first step of the retrieval ([section 2a](#)) is used to calculate the thermal-wind-balanced reference state. The Cartesian wind components are converted to radial and tangential wind components, and the tangential wind is averaged azimuthally. The vertical temperature and pressure profiles needed as boundary conditions for the inward integration of the thermal wind equation are calculated from the azimuthally averaged temperature and pressure fields at the outer edge of the SAMURAI domain. Ideally, if the domain is large enough, then the pressure surfaces become horizontal at the edge of the domain and the balanced state is identical to a hydrostatic environmental vertical profile. For smaller domains the vertical profile can be derived from an average of in situ measurements at the outer edge of the retrieval domain.

The assumption of the gradient-wind balance is not justified in the boundary layer because of increased amounts of friction. We use a simple parameterization of the wind field in the boundary layer to minimize the introduction of errors. The tangential wind field is assumed to be constant with height in the boundary layer, assuming the values of the wind field at 2 km altitude. This simple parameterization minimizes the effects of the boundary layer wind field on the temperature and pressure retrievals. However, its simplicity also precludes the interpretation of the retrieved temperature and pressure perturbations within the boundary layer.

### c. Thermodynamic retrieval with SAMURAI-TR

The thermodynamic retrieval shares many technical elements with SAMURAI. It also minimizes a cost function using a Galerkin approach, with cubic B-spline finite elements as a basis, and it has the same spatial filtering capabilities as SAMURAI. Pseudo-observations

of variable gradients can be used directly as retrieval input, avoiding the direct solution of an elliptic equation. This section outlines the derivation of the set of equations used to construct the cost function. Minimizing this cost function then yields an estimate of the most likely thermodynamic state of the atmosphere given the radar-derived winds.

Similar to previous thermodynamic retrieval techniques, we start with the inviscid momentum equations in Cartesian coordinates on a constant  $f$ -plane, neglecting momentum transport by precipitation, frictional forces, and subgrid-scale processes:

$$\frac{D\mathbf{u}}{dt} + f\mathbf{k} \times \mathbf{u} + \frac{1}{\rho} \nabla p + g\mathbf{k} = 0, \quad (5)$$

where  $\mathbf{u}$  denotes the three-dimensional wind in vector form and  $\mathbf{k}$  denotes the vertical unit vector. We analyze the effect of the inviscid assumption later in the verification section. To adapt the equations into a numerically solvable form, the pressure gradient terms are transformed into nondimensional expressions by using the Exner function  $\pi = (p/p_0)^{R_d/c_p}$ . Density is expressed in terms of pressure, temperature, and moisture using density potential temperature  $\theta_\rho$ .

The thermodynamic variables are separated into basic state and perturbations, where the basic state, denoted by the overbar, is a function of  $r$  and  $z$  only:

$$\theta_\rho = \bar{\theta}_\rho(r, z) + \theta'_\rho \quad \text{and} \quad (6)$$

$$\pi = \bar{\pi}(r, z) + \pi'. \quad (7)$$

Our basic (or reference) state was chosen to be in thermal wind balance:

$$c_p \bar{\theta}_\rho \frac{\partial \bar{\pi}}{\partial z} = -g \quad \text{and} \quad (8)$$

$$\frac{\bar{V}_T^2}{r} + f\bar{V}_T = c_p \bar{\theta}_\rho \frac{\partial \bar{\pi}}{\partial r}, \quad (9)$$

where the gradient wind balance relationship is expressed in cylindrical coordinates using the tangential velocity  $\bar{V}_T$ . The hydrostatic balance relationship can be used to simplify the vertical momentum equation. The horizontal derivatives of the reference-state pressure field ( $\partial \bar{\pi}/\partial x$  and  $\partial \bar{\pi}/\partial y$ , calculated in section 2b) can be used to specify the horizontal gradients of the basic-state pressure field. The terms in the momentum equations are expanded into basic state and perturbations, and the nonlinear terms are neglected in the vertical momentum equation. Initial tests of the retrieval with only these three modified momentum equations showed good results for the pressure retrieval but unsatisfactory results for the temperature retrieval. The vertical momentum equation links the pressure and

temperature fields together; however, it is the only equation containing  $\theta'_\rho$ , and the pressure term in the vertical momentum equation is several orders of magnitude larger than the temperature term. Thus, variations in the temperature field essentially do not affect the cost function, yielding a temperature field that is close to zero everywhere in the domain. To mitigate this problem, we followed Roux (1985) and combined the derivatives of the horizontal and vertical momentum equations to add two more equations containing only  $\theta'_\rho$  terms. This yields the final set of equations in component form, containing two equations for  $\pi'$ , two equations for  $\theta'_\rho$ , and one equation for both variables:

$$\frac{1}{c_p \bar{\theta}_\rho} \left( \frac{\partial u}{\partial t} + u \frac{\partial u}{\partial x} + v \frac{\partial u}{\partial y} + w \frac{\partial u}{\partial z} - fv \right) + \frac{\partial \bar{\pi}}{\partial x} = A = -\frac{\partial \pi'}{\partial x}, \quad (10)$$

$$\frac{1}{c_p \bar{\theta}_\rho} \left( \frac{\partial v}{\partial t} + u \frac{\partial v}{\partial x} + v \frac{\partial v}{\partial y} + w \frac{\partial v}{\partial z} + fu \right) + \frac{\partial \bar{\pi}}{\partial y} = B = -\frac{\partial \pi'}{\partial y}, \quad (11)$$

$$\frac{1}{c_p \bar{\theta}_\rho} \left( \frac{\partial w}{\partial t} + u \frac{\partial w}{\partial x} + v \frac{\partial w}{\partial y} + w \frac{\partial w}{\partial z} \right) = C = -\frac{\partial \pi'}{\partial z} + \frac{g}{c_p \bar{\theta}_\rho} \theta'_\rho, \quad (12)$$

$$\frac{-c_p \bar{\theta}_\rho^2}{g} \left( \frac{\partial A}{\partial z} - \frac{\partial C}{\partial x} \right) = D = \frac{\partial \theta'_\rho}{\partial x}, \quad \text{and} \quad (13)$$

$$\frac{-c_p \bar{\theta}_\rho^2}{g} \left( \frac{\partial B}{\partial z} - \frac{\partial C}{\partial y} \right) = E = \frac{\partial \theta'_\rho}{\partial y}. \quad (14)$$

Similar to friction and subgrid-scale terms, the time tendency terms are difficult to quantify from real data. Hence, we will neglect them in general, with further analysis of that assumption described later in the verification section. To solve these equations, we minimize an incremental form of a variational cost function using a conjugate gradient algorithm identical to the approach used in SAMURAI. The control variable state vector takes the form of  $\mathbf{x} = \{\pi', \theta'_\rho\}$ .

With the exception of Eq. (12), the retrieval equations contain spatial derivatives of the variables of interest rather than the variables of interest themselves. Thus, the retrieval solution is not unique and could be satisfied by adding an arbitrary constant function of height, such that  $\pi' + F(z)$  and  $\theta'_\rho + \partial F(z)/\partial z$  are also valid solutions. In the current framework,  $F(z)$  represents a systematic, horizontally homogeneous departure from thermal-wind balance at each vertical level. By defining the reference state in a physically meaningful way, the strong physical constraints of the rapidly rotating vortex dictate that these departures are usually small (Willoughby 1990) and asymmetric, resulting in a near-zero horizontal average at

each level. The use of the horizontally varying balanced reference state also removes the requirement for an in situ vertical profile within the retrieval domain to resolve the integration constants, allowing the profile to be prescribed at the outer edge of the domain from an environmental reference. Since the perturbation retrieval depends only weakly on the absolute magnitude of the mean density potential temperature and is independent of the absolute magnitude of the mean pressure, the retrieved perturbations are not sensitive to the choice of the environmental vertical profile.

In addition to the abovementioned physical constraints, the three-dimensional cubic B-splines and spatial filtering effectively couple the vertical levels and limit the allowed shape of any constant function of height in the numerical solution. Because of both physical and numerical constraints, the likelihood of a large unresolved height-dependent constant function is low in this method, but it cannot be explicitly determined. Hence, we assume—a priori—that there are no additional constants and that the horizontally averaged perturbations, denoted here as  $\langle \pi' \rangle$  and  $\langle \theta'_p \rangle$ , are zero. This assumption will be analyzed further in the verification section.

There are several distinctions in the approach of SAMURAI-TR compared to previous methods. The reference-state definition varies with radius and height to account for the strong mean thermodynamic gradients associated with a rapidly rotating vortex. The cost function minimization algorithm has an efficient filtering mechanism to control the resolved scales, eliminating the need for smoothing penalty constraints in the cost function itself. Because of the cubic B-spline basis, the first and second spatial derivatives of the structure in all three dimensions are exact for a given set of nodal coefficients, providing higher numerical accuracy than a finite-difference representation of the derivatives. The variational analysis is obtained by solving directly for the nodal coefficients that give consistent pressure and temperature gradients in Eqs. (10)–(14), indirectly producing a three-dimensional function that represents the pressure and temperature itself. Using this approach, the classical problem of linking vertical levels in the retrieval is accomplished without the necessity of microphysical constraints (Roux et al. 1993) or the thermodynamic equation (Liou et al. 2003). A thorough verification of this new thermodynamic retrieval methodology is presented in the next chapter.

### 3. Retrieval evaluation

The performance of SAMURAI-TR is assessed and its uncertainties are quantified using a WRF simulation

of Hurricane Rita (2005). The WRF simulation provides both kinematic and thermodynamic variables. Thus, it is possible to evaluate the thermodynamic quantities derived from the model's kinematic fields with the thermodynamic fields of the model.

#### *a. Observing system experiment*

The simulation uses version 3.6.1 of WRF with four nested domains of 18-, 6-, 2-, and 2/3-km resolution, and 300, 250, 250, and 400 grid points square, respectively. The three inner domains are vortex following using the pressure minimum at 700 hPa. The simulation uses the following physics parameterizations: Rapid Radiative Transfer Model (RRTM) longwave radiation (Mlawer et al. 1997), Dudhia shortwave radiation (Dudhia 1989), the Noah land surface model (Ek et al. 2003), the Yonsei University boundary layer scheme (Hong et al. 2006), Thompson aerosol-aware micro-physics (Thompson and Eidhammer 2014), and modified surface fluxes for tropical cyclones (Garratt formulation; Davis et al. (2008)). The outer two domains use the Kain–Fritsch cumulus parameterization (Kain and Fritsch 1990), while the inner two domains are convective permitting. The WRF simulation was run from 18 to 23 September 2005, and captured both the period of rapid intensification and the secondary eyewall formation of Hurricane Rita.

Figure 1 shows the evolution of Hurricane Rita in the WRF simulation from 0000 UTC 20 September to 1800 UTC 21 September, during which Rita strengthened from a category 1 to a category 5 hurricane. The evaluation of the retrieval will focus on this period. At 0000 UTC 20 September, the simulated storm is a category 1 hurricane. The convection is concentrated in a broad region in the southern half of the domain, at a radius of about 30 km. By 0000 UTC 21 September, Rita strengthens to a category 3 hurricane. The eyewall is concentric, with the most active convection to the south. Rita further strengthens and becomes a category 5 hurricane at 1800 UTC 21 September. The radius of the eyewall shrinks to about 20 km, and a secondary eyewall is visible at a radius of about 50 km.

The sigma-level output of the innermost WRF domain was converted to Cartesian coordinates using SAMURAI for the eight times shown in Fig. 1, equivalent to step 1 of the retrieval method. In contrast to a wind field derived from observations, however, the wind field here does not contain any errors. The resolution of the Cartesian grid is 1 km in the horizontal and 0.5 km in the vertical, with a domain size of  $150 \text{ km} \times 150 \text{ km} \times 16 \text{ km}$ . The gradient-wind-balanced reference state is calculated from the gridded SAMURAI analysis according to step 2 of the retrieval method. The wind field of step 1 and

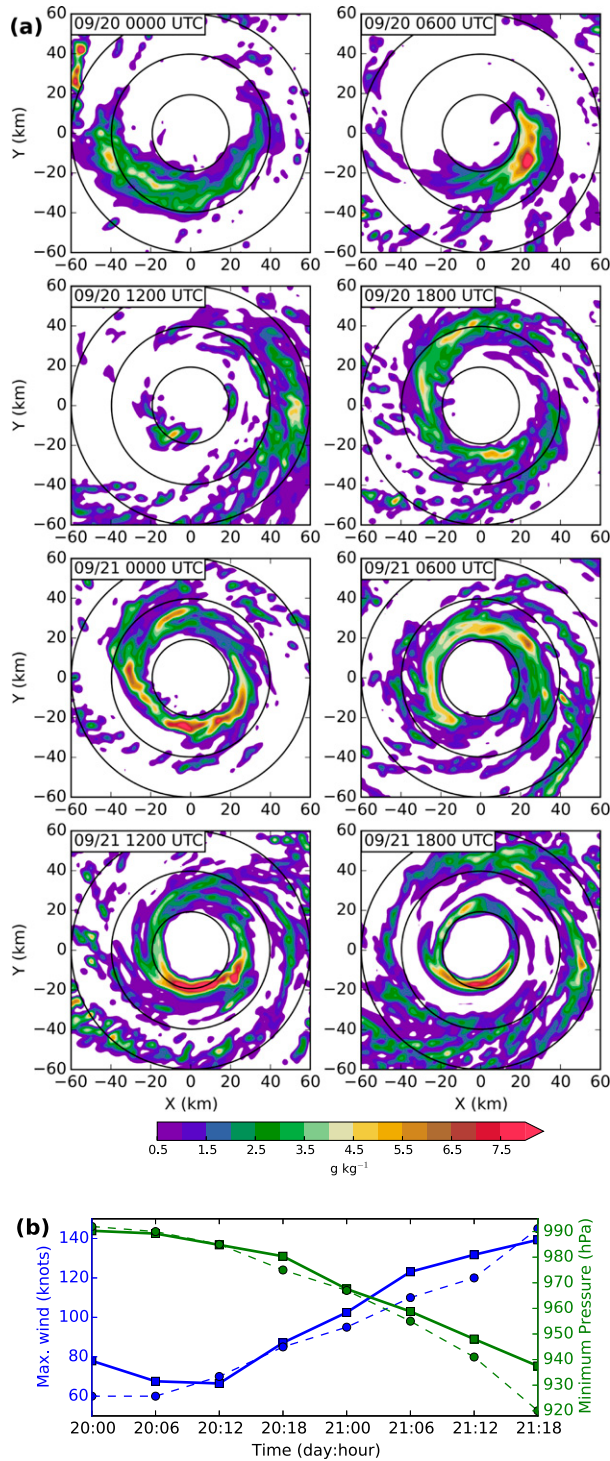


FIG. 1. (a) Horizontal cross sections of WRF precipitation mixing ratio at 2 km altitude (shaded,  $\text{g kg}^{-1}$ ) from 0000 UTC 20 Sep 2005 to 1800 UTC 21 Sep in increments of 6 h. Range rings of 20, 40, and 60 km around the storm center (black solid circles). (b) WRF maximum wind speed at 2 km altitude (blue solid, kt) and best track 1-min sustained wind speed (blue dashed, kt), and WRF minimum sea level pressure (green solid, hPa) and best track minimum sea level pressure (green dashed, hPa) for the times shown in (a).

the reference pressure and temperature fields of step 2 are then used as input for retrieving the temperature and pressure perturbations with SAMURAI-TR in step 3.

### b. Pressure retrieval

SAMURAI-TR solves for normalized pressure perturbation  $\pi'$  and density potential temperature perturbation  $\theta'_\rho$ . To facilitate the interpretation of the pressure retrieval results, the retrieved  $\pi'$  fields are postprocessed and displayed here in terms of perturbation pressure  $p'$  in units of hectopascals instead of the unitless quantity  $\pi'$ . The first and last snapshots in Fig. 1 are used to illustrate the retrieval performance at different storm intensities. A comparison of the WRF and the retrieved total pressure  $p$  (Figs. 2a,b) at the earlier time (0000 UTC 20 September) shows very good overall agreement between the retrieved pressure and the WRF pressure, with a prominent pressure drop toward the center of the storm.

The total pressure  $p$  is the sum of the mean pressure  $\bar{p}$  calculated from the mean tangential wind field in step 2 of the retrieval method and the pressure perturbation  $p'$  retrieved with SAMURAI-TR in step 3. The spatial correlation coefficient (Liou 2001,

$$\text{SCC}(A) = \frac{(A_r - \bar{A}_r)(A_t - \bar{A}_t)}{\sqrt{(A_r - \bar{A}_r)^2(A_t - \bar{A}_t)^2}},$$

with the domain average  $\bar{A}$ , and the subscripts  $r$  and  $t$  denoting the “retrieved” and “true” quantities, respectively) of the total pressure at this earlier time is a perfect 1.000 (Table 1), signifying excellent similarity between WRF and the retrieval. The retrieval performs slightly better at 4 km than at 8 km, which can be attributed to issues with the boundary conditions caused by the asymmetric pressure structure at outer radii at 8 km altitude. The perturbation pressure  $p'$  reveals the small variations in the pressure field that are largely masked in the total pressure field by the prominent radial pressure drop. The horizontal cross sections of  $p'$  at 4 and 8 km (Figs. 2c,d) show that the retrieval correctly identifies the regions of positive and negative perturbations along with the perturbation magnitudes. At 4 km (Fig. 2c), both WRF and the retrieval show a broad positive region, accompanied by two small negative areas. At 8 km (Fig. 2d), the retrieval correctly places the negative perturbation just inside the area of convection, with a positive perturbation toward the northeast. The weak perturbations toward the domain boundaries are not resolved. Vertical cross sections (Figs. 2e,f) show good agreement between the WRF pressure perturbations and the retrieved pressure perturbations. The locations and magnitudes are generally depicted correctly, with small discrepancies toward the

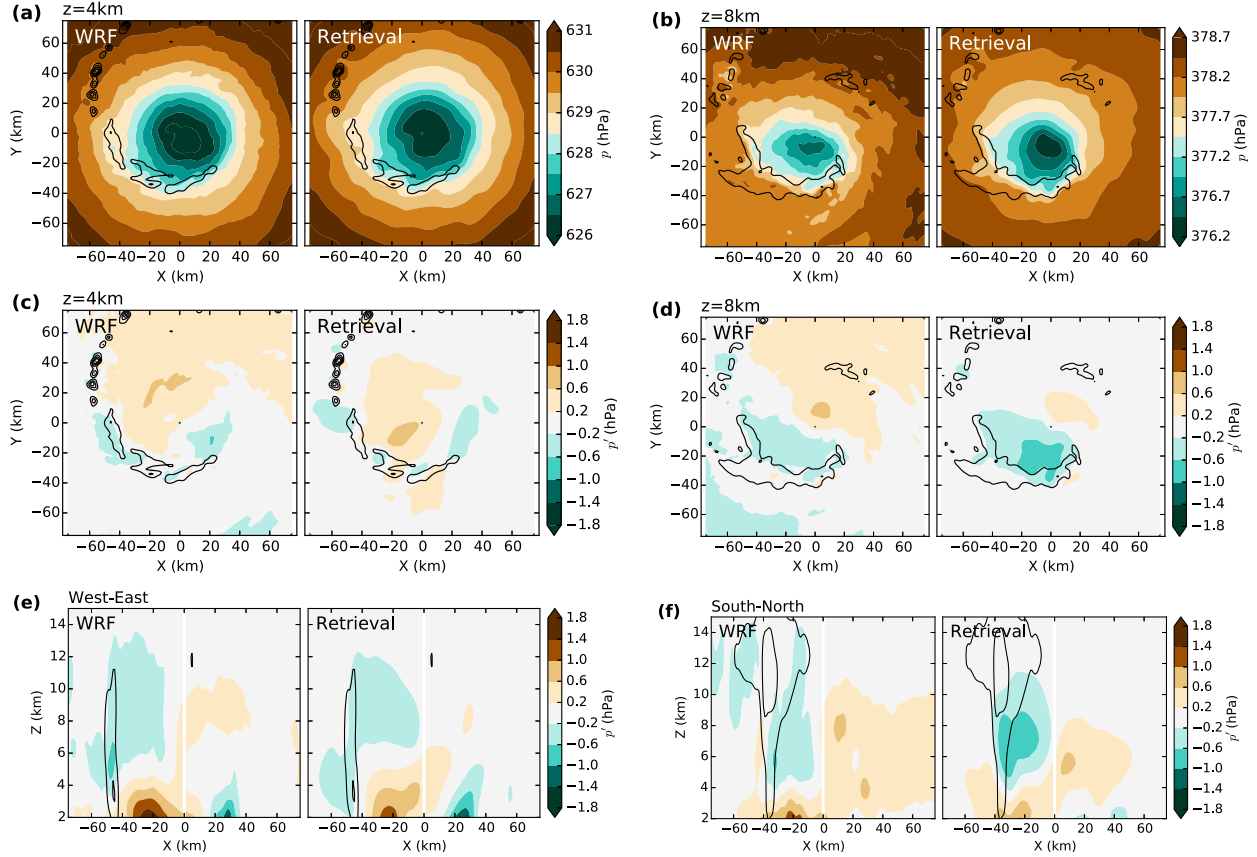


FIG. 2. Comparison of WRF output and pressure retrieval output for 0000 UTC 20 Sep 2005. (a),(b) Horizontal cross sections of  $p$  (shaded, hPa), and (c),(d) horizontal and (e),(f) vertical cross sections of  $p'$  (shaded, hPa) at (a),(c) 4- and (b),(d) 8 km altitude. Contours of precipitation mixing ratio ( $\text{g kg}^{-1}$ , increments of  $3 \text{ g kg}^{-1}$ ) are included for easier comparison.

boundaries where the retrieval tends toward zero and the WRF simulation displays nonzero values.

At the latter time, 1800 UTC 21 September (Fig. 3), the magnitude of the mean pressure drop and the magnitude of the perturbations are much larger. The mean pressure drop at 4 km is about 25 hPa compared to 5 hPa at the earlier time, and the perturbations now cover more than twice the range compared to the earlier time. Again, the retrieved total pressure  $p$  (Figs. 3a,b) shows very good agreement with the WRF simulation at both vertical levels. The retrieval correctly identifies the pronounced wavenumber-1 pattern in  $p'$  at both vertical levels (Figs. 3c,d), with the maximum negative perturbation collocated with the ring of convection at 4 km altitude. As at the earlier time, the perturbations toward the boundaries are smaller than in the WRF simulation. The vertical cross sections (Figs. 3e,f) show the collocation of the negative pressure perturbations with the eyewall convection at all vertical levels and the positive perturbations located slightly further radially outward, in both the WRF simulation and the retrieval.

Cross sections for the earlier and the latter times indicate a good performance of the pressure retrieval. Statistical measures for all eight different times confirm the performance (Table 1). The root-mean-square (RMS) of  $p'$  is used as a measure for the perturbation magnitude. The RMS of the retrieval and the WRF simulation are of similar magnitude and increase with increasing strength of the vortex, with the retrieval RMS increasing from 0.16 to 0.65 hPa and the WRF RMS increasing from 0.22 to 0.82 hPa. The root-mean-square error (RMSE) ranges from 0.16 to 0.36 hPa. The spatial correlation coefficient for the total pressure shows a perfect score of 1.0 at a precision of three significant digits. The SCC for the pressure perturbations is always above 0.58, and it generally increases with increasing storm intensity. The two times that perform the worst (1800 UTC 20 September and 0000 UTC 21 September) exhibit low RMS magnitudes, which indicates that the retrieval is more challenging when the perturbations are small. The last column of the table adds a metric to evaluate how well the retrieval is able to correctly identify the areas

TABLE 1. Statistics for the evaluation of the pressure retrieval against the WRF output in terms of  $p$  (hPa) and  $p'$  (hPa) for eight different times (0000 UTC 20 Sep 2005–1800 UTC 21 Sep 2005): RMS of  $p'$  for retrieval (RMS TR) and WRF output (RMS WRF), RMSE of  $p'$  (RMSE), SCC for  $p$  and  $p'$ , and the percentage of grid points with the correctly retrieved sign (% sign). See text for details about the calculation of the SCC and the % sign.

Time and date	RMS TR	RMS WRF	RMSE	SCC $\pi$	SCC $\pi'$	% sign
0000 UTC 20 Sep	0.17	0.23	0.19	1.000	0.58	90
0600 UTC 20 Sep	0.16	0.22	0.16	1.000	0.67	93
1200 UTC 20 Sep	0.26	0.32	0.21	1.000	0.82	87
1800 UTC 20 Sep	0.17	0.28	0.22	1.000	0.61	84
0000 UTC 21 Sep	0.19	0.25	0.19	1.000	0.68	88
0600 UTC 21 Sep	0.35	0.48	0.25	1.000	0.87	90
1200 UTC 21 Sep	0.66	0.81	0.31	1.000	0.93	86
1800 UTC 21 Sep	0.65	0.82	0.36	1.000	0.92	93

with significant positive or negative perturbations. The “% sign” metric calculates the percentage of the grid points for which the retrieval correctly determines the sign of the perturbation, using only grid points where the retrieved (positive or negative) pressure perturbation exceeds 0.2 hPa (which is the shading threshold for all pressure perturbation plots). The metric shows that the sign is determined correctly for over 84% of the grid points in all cases, exceeding 90% in four cases. The two times with lower SCC values (1800 UTC 20 September and 0000 UTC 21 September) also verify at over 84%, again pointing to the fact that the perturbations were small in these cases. Overall, both visual inspection and statistical evaluation confirm the good performance of the pressure retrieval, but the error analysis suggests caution should be used in scientific interpretation of weak perturbations.

### c. Temperature retrieval

The temperature retrieval performance is examined in detail for the same two times as the pressure retrieval, 0000 UTC 20 September and 1800 UTC 21 September. The total density potential temperature  $\theta_p$  is the sum of the mean density potential temperature  $\bar{\theta}_p$  calculated from the mean tangential wind field in step 2 of the retrieval method and the density potential temperature perturbations  $\theta'_p$  retrieved with SAMURAI-TR in step 3.

At the earlier time, 0000 UTC 20 September, a comparison between WRF and  $\theta_p$  at 4 km (Fig. 4a) shows that the retrieval correctly identifies the location of the temperature maximum and the overall structure of the temperature field. The temperature maximum in the WRF simulation is shifted southward at 8 km compared to the lower level, which is also reflected in the retrieval (Fig. 4b). Subtracting off the balanced temperature contribution

reveals a wavenumber-1 pattern in  $\theta'_p$  at 4 km (Fig. 4c), with negative perturbations just inside the convection to the southwest and positive perturbations northeast of it. The retrieval correctly identifies this wavenumber-1 pattern, but some small discrepancies occur. The retrieval is smoother than the WRF simulation and underestimates the small negative perturbation toward the southwestern boundary. The perturbations at 8 km (Fig. 4d) are relatively small. Both the WRF simulation and the retrieval show an extended negative area in the northern half of the domain and small positive areas within the region of convection. Vertical cross sections (Figs. 4e,f) show a good agreement of the WRF simulation and the retrieval up to about 8 km. Above that, the retrieved temperature perturbations in the west–east cross section seem to have a slight positive bias. The south–north cross section shows a pronounced positive perturbation collocated with the maximum reflectivities at 9–12-km height that is not apparent in the WRF simulation.

At the latter time, 1800 UTC 21 September, the total temperature difference between the domain boundary and the center is approximately 20 K, compared to 10 K at the earlier time, and the magnitudes of the temperature perturbations increase from about 1.5 to over 3 K. The retrieval of the total density potential temperature is very consistent with the verification data (Figs. 5a,b). Subtracting off the balanced temperature contribution shows that the main regions of perturbation are linked to the eyewall, with a narrow arc of positive values toward the northwest of the center and a narrow arc of negative values toward the southeast but at a slightly larger radius. This pattern is prominent in both the WRF simulation and the retrieval at 4 km (Fig. 5c) and at 8 km (Fig. 5d). The pattern outside the eyewall region is close to zero in the WRF simulation and the retrieval at 8 km, but it differs at 4 km. The WRF retrieval has mostly negative values outside the eyewall region, whereas the retrieval shows a more diverse pattern. The vertical cross sections show that the temperature anomalies are closely tied to the convection. In the western and northern eyewall, the positive anomalies are located inside the eyewall in both the WRF simulation and the retrieval (Figs. 5e,f). In the eastern and southern eyewall, the negative anomalies are collocated with the convection in both the WRF simulation and the retrieval. Small discrepancies between the WRF simulation and the retrieval are apparent in the center, where the positive temperature perturbation is located higher up (8–11 km) in the retrieval than in the WRF simulation (6–8 km). Moreover, the columns of positive perturbation in the western and northern eyewall are deeper in the retrieval, whereas the WRF simulation has a minimum at around 10-km height and increasing values above.

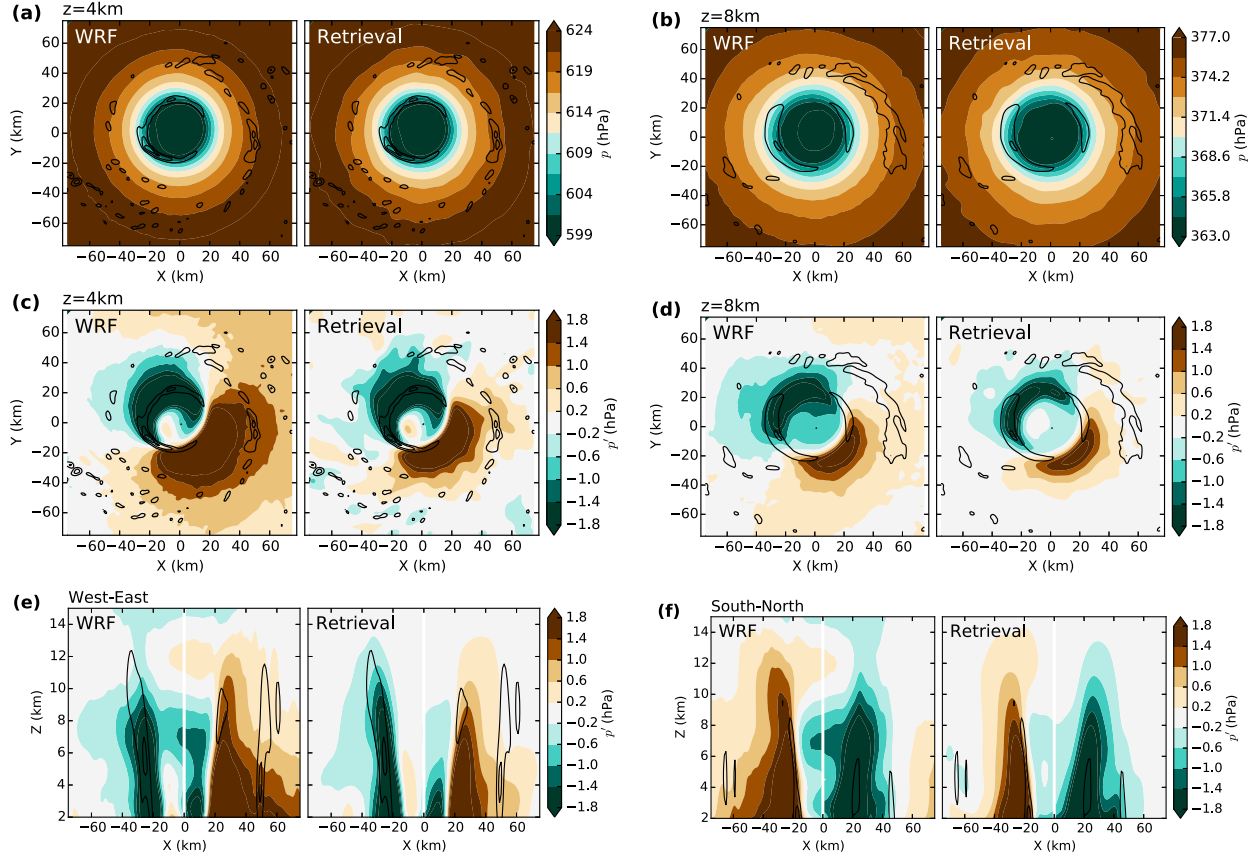


FIG. 3. Comparison of WRF output and pressure retrieval output for 1800 UTC 21 Sep 2005 as in Fig. 2.

Table 2 summarizes the performance of the temperature retrieval. SAMURAI-TR does show skill, especially at higher storm intensities. However, the verification statistics indicate that the temperature retrieval is more challenging than the pressure retrieval. This could be expected, since the temperature perturbation gradients are related to the second-order derivatives of the wind components, whereas the pressure perturbation gradients are related to their first-order derivatives. The retrieval RMS values for  $\theta'_p$  range from 0.38 to 0.73 K; the WRF simulation RMS values are slightly higher, ranging from 0.60 to 0.92 K. The RMSE values are well below 1 K, ranging from 0.56 to 0.85 K. The spatial correlation of  $\theta'_p$  is almost perfect with a value of 0.999 in all eight cases. The spatial correlation of  $\theta'_p$  reaches values of 0.19 to 0.61. These values are slightly lower than the SCC values for  $\pi'$ . The last column again contains the metric calculating the percentage of points where the retrieval correctly determines the sign of the perturbation but only using points where the retrieved (positive or negative) temperature perturbation exceeds 0.5 K (which is also the shading threshold in all the temperature perturbation plots). The percentage of correctly identifying the sign is

well above 50% in every case and as high as 85%. The lowest scores occur at the same two times as for the pressure retrieval, and again the RMS magnitudes of the retrieved quantity are comparatively low in these cases, indicating that the retrieval performance is poorer when the perturbations are weak.

#### d. Sensitivity tests

The evaluation of SAMURAI-TR in the previous section yielded good accuracy. The sensitivity of these results to the formulation of the time tendency term, to the assumption that there is no unresolved integration constant, and to the addition of random noise is tested in this section.

##### 1) TIME TENDENCY TERM

Guimond et al. (2011) found the results of their latent heat retrieval to be quite sensitive to the time tendency term. While it is desirable to include this term in the retrieval, it is usually not feasible to include when working with airborne radar data. A complete scan of the eyewall using a tail Doppler radar takes on the order of 20 min. Even if the flight track allows for two consecutive complete scans, the time tendency term calculated from that is

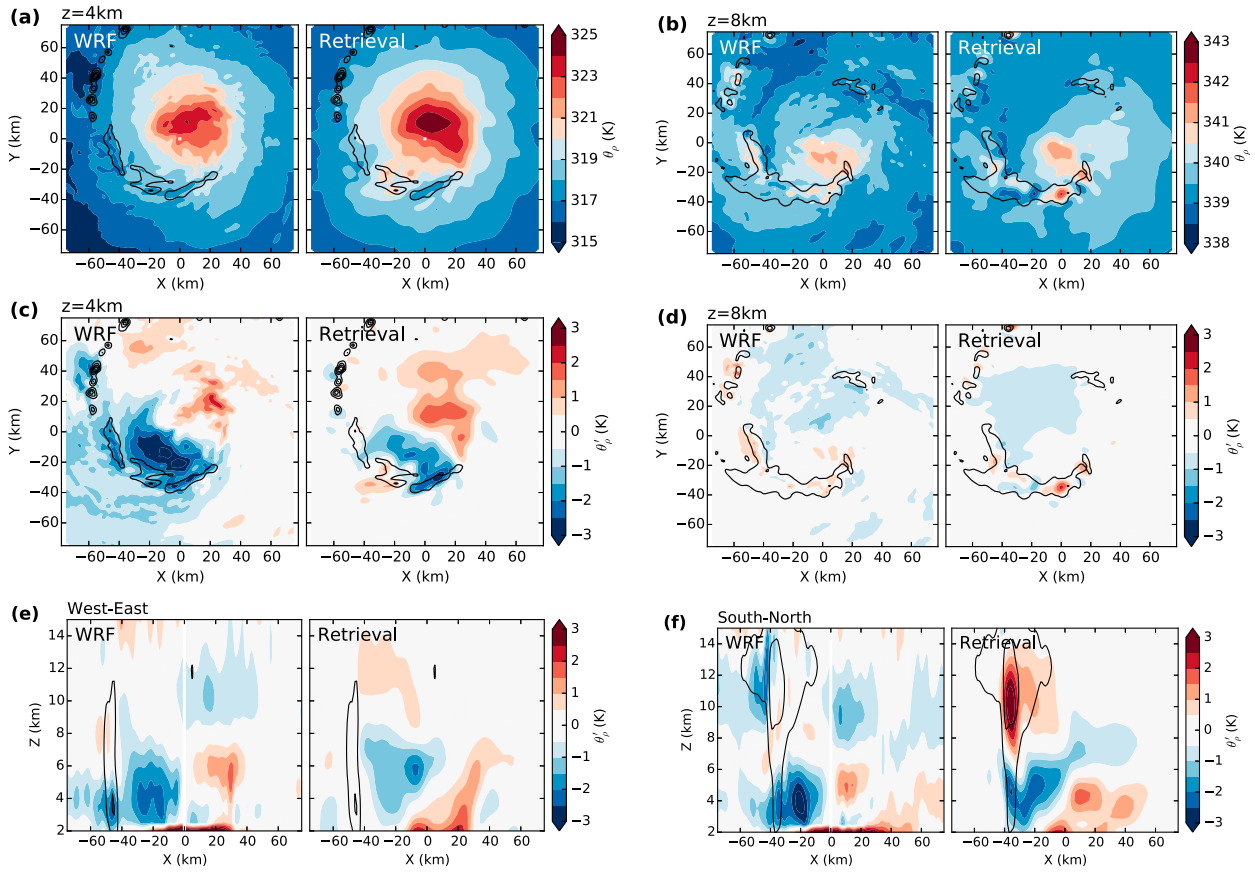


FIG. 4. Comparison of WRF output and temperature retrieval output for 0000 UTC 20 Sep 2005. (a),(b) Horizontal cross sections of  $\theta_p'$  (shaded, K), and (c),(d) horizontal and (e),(f) vertical cross sections of  $\theta_p'$  (shaded, K) at (a),(c) 4 and (b),(d) 8 km altitude. Contours of precipitation mixing ratio ( $\text{g kg}^{-1}$ , increments of  $3 \text{ g kg}^{-1}$ ) are included for easier comparison.

very small because of the large lag between the two scans. However, it is important to investigate the shortcomings that result from neglecting the time tendency term in the retrieval. Retrievals, including the time tendency term, were performed, and the time tendency term was calculated from the forward difference for two different intervals, 1 and 20 min. A comparison of the retrieval output for the different intervals with the WRF simulation and a retrieval run with no time tendency term included shows that the time tendency term changes the retrieval output only slightly (Figs. 6, 7). The overall patterns of all three retrievals look very similar; however, the 1-min retrieval captures more detail.

At the earlier time, the 1-min retrieval at 4 km altitude (Fig. 6a) resolves the area of positive perturbation located inward of the convective band toward the upper boundary, whereas this area is not resolved in the 20-min retrieval or the retrieval without time tendency term. Similarly, at 8 km altitude (Fig. 6b), the 1-min retrieval is the only retrieval that shows structure within the area of negative perturbations north of the center. The other

retrievals show a broad area of negative values. The differences between the 20-min retrieval and the retrieval without time tendency term are subtle.

During the more intense phase of the storm, 1800 UTC 21 September (Fig. 7), the three retrievals again look very similar. At 4 km (Fig. 7a), none of the retrievals correctly depict the broad area of negative perturbations outside the eyewall that is apparent in the WRF simulation. However, they all show an area of positive perturbations spiraling outward outside the northwestern part of the eyewall and an area of negative values in the northwestern corner of the domain. The 1-min retrieval is relatively smooth, whereas the 20-min retrieval is more cellular. At 8 km (Fig. 7b), nonzero perturbations occur mainly in and around the eyewall. All three retrievals locate these perturbations correctly; however, they also incorrectly place some smaller-magnitude perturbations outside the eyewall region.

Neglecting the time tendency term degrades the quality of the retrieval only slightly. The only viable option with real airborne radar data would be to add a

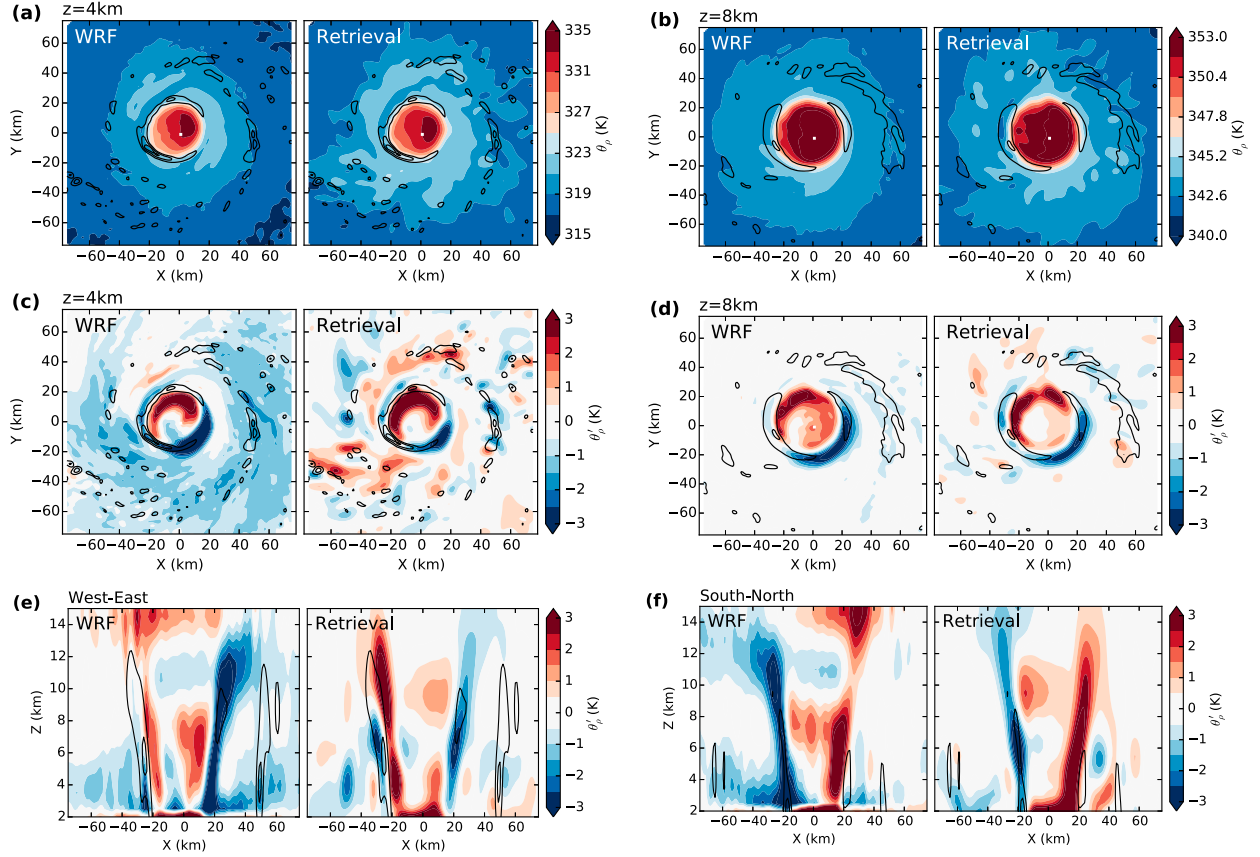


FIG. 5. Comparison of WRF output and temperature retrieval output for 1800 UTC 21 Sep 2005 as in Fig. 4.

20-min (or even longer period) time tendency term, but adding this term basically did not show any effect with the WRF tests. Value could potentially be added by including the tendency term in cases with ground-based Doppler retrievals with better temporal resolution.

## 2) HEIGHT-DEPENDENT ADDITIONAL CONSTANTS

As stated in section 2c, our approach assumes that there are no additional height-dependent constants that have to be added to either the retrieved  $p'$  and/or  $\theta'_p$  as a result of the physical and numerical constraints of the method. The validity of this assumption is tested by computing the average perturbations  $\langle p' \rangle$  and  $\langle \theta'_p \rangle$  at each vertical level for the WRF simulation and the retrieval. The difference between the average perturbation of the WRF simulation and that of the retrieval represents the height-dependent constant and systematic departure from thermal wind balance at that level. By adding this constant to the retrieved fields and computing the statistics of a “bias corrected” field, we can quantify the effect of neglecting the constant. As expected, the height-dependent average perturbations for the retrieval are zero or close to zero at all times (Tables 3, 4), but they are nonnegligible in some

instances in the WRF simulation. For the majority of the eight times used for the evaluation, the average perturbations are close to zero, but for 0000 UTC 20 September, 1800 UTC 20 September, and 1800 UTC 21 September, the absolute value of the average  $\langle \theta'_p \rangle$  exceeds 0.19 K.

In the majority of the cases, the statistics improve slightly by knowing the constant. The statistics improve the most for the cases that performed worst in the original retrieval. The pressure retrieval shows a reduction of the average RMSE of  $p'$  from 0.24 to 0.20 hPa, an increase of the average SCC of  $p'$  from 0.76 to 0.82, and an increase of the average % sign from 89% to 93%. The temperature retrieval shows a reduction of the average RMSE of  $\theta'_p$  from 0.68 to 0.58 K, an increase of the average SCC of  $\theta'_p$  from 0.44 to 0.63, and an increase of the average percent sign from 71% to 84%. The improvement is largest for the times that performed the worst in the original temperature retrieval, 1800 UTC 20 September and 0000 UTC 21 September. However, in most cases, the retrieval is degraded only slightly by neglecting the unresolved height-dependent additional constants. Hence, the assumption that  $\langle p' \rangle$  and  $\langle \theta'_p \rangle$  are zero is justifiable but yields some small errors.

TABLE 2. Statistics for the evaluation of the temperature retrieval against the WRF output in terms of  $\theta_p$  (K) and  $\theta'_p$  (K) for eight different times (0000 UTC 20 Sep 2005–1800 UTC 21 Sep 2005): RMS of  $\theta'_p$  for retrieval (RMS TR) and WRF output (RMS WRF), RMSE of  $\theta'_p$  (RMSE), SCC for  $\theta_p$  and  $\theta'_p$ , and the percentage of grid points with the correctly retrieved sign (% sign).

Time and date	RMS TR	RMS WRF	RMS RMSE	SCC $\theta_p$	SCC $\theta'_p$	% sign
0000 UTC 20 Sep	0.43	0.66	0.59	0.999	0.50	80
0600 UTC 20 Sep	0.53	0.78	0.62	0.999	0.61	85
1200 UTC 20 Sep	0.43	0.61	0.56	0.999	0.47	77
1800 UTC 20 Sep	0.38	0.60	0.65	0.999	0.19	59
0000 UTC 21 Sep	0.45	0.72	0.75	0.999	0.25	59
0600 UTC 21 Sep	0.54	0.74	0.73	0.999	0.38	68
1200 UTC 21 Sep	0.73	0.88	0.73	0.999	0.60	72
1800 UTC 21 Sep	0.71	0.92	0.84	0.999	0.53	70

### 3) RANDOM NOISE

Observations always contain a certain degree of noise, and the calculation of spatial gradients and the neglect of subgrid and friction terms can add numerical error in the retrieval. For a well-resolved Doppler geometry, the uncertainty in the wind field should be less than  $2 \text{ m s}^{-1}$  (Hildebrand et al. 1996). The effect of random noise on the accuracy of the thermodynamic retrieval is tested by adding Gaussian noise to each of the three wind components of the WRF input, using the Box–Muller method with a standard deviation of  $1 \text{ m s}^{-1}$  for a

realistic minimal error test and with a standard deviation of  $2 \text{ m s}^{-1}$  for a larger error test. The spatial derivatives of the wind field components, used as input for the retrieval along with the wind field itself, are calculated from these noisy wind fields.

Visual comparison of the retrieved pressure perturbations and density potential temperature perturbations with the WRF fields (Fig. 8) shows that the addition of noise degrades the retrieval results only marginally. The perturbation patterns in the eyewall region are very similar for all three retrievals, with the added noise acting to marginally reduce the absolute magnitudes of the retrieved perturbations. In the outer regions, small discrepancies between the three retrievals are visible, in this case degrading the quality of the temperature retrieval but actually improving the quality of the weak pressure perturbations.

The statistics comparing the retrieved perturbation fields to the WRF fields show very similar numbers for the retrievals with added noise and for the noise-free retrieval. The RMSE value of pressure perturbations, averaged over all eight times, is identical for noise-free and noisy retrievals with an accuracy of two significant digits after the decimal point. The %-sign value of normalized pressure perturbations, averaged over all eight times, is insignificantly higher for the  $1 \text{ m s}^{-1}$  noise retrieval and only 0.02 lower for the  $2 \text{ m s}^{-1}$  noise retrieval. For the density potential temperature perturbations, the RMSE

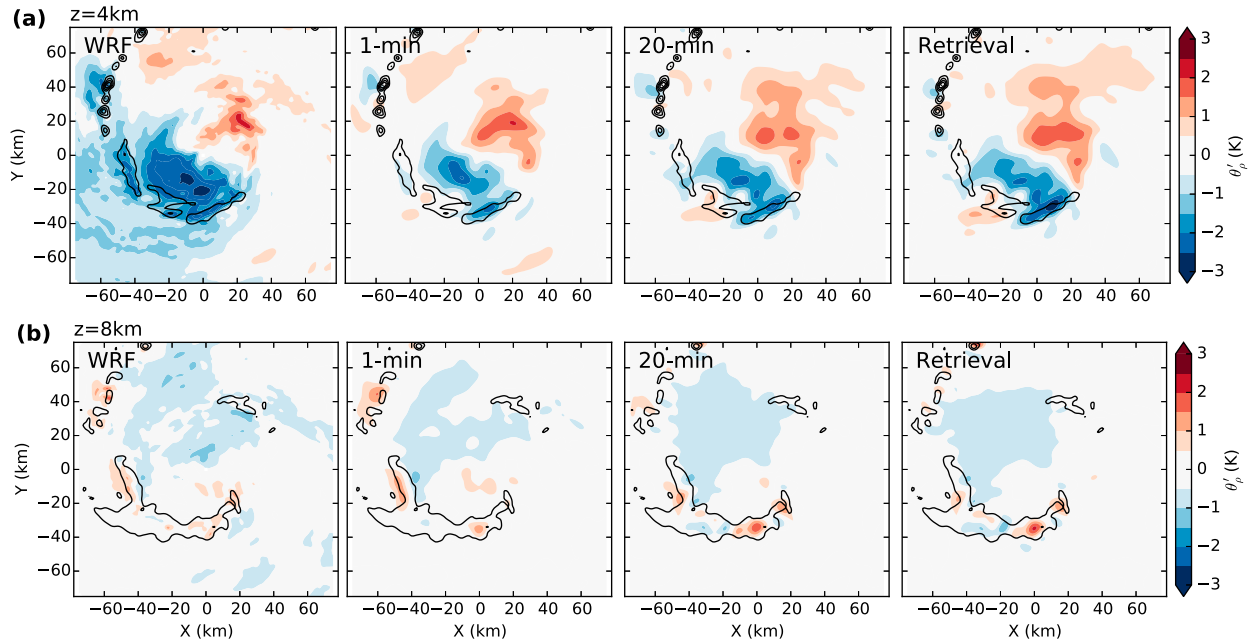


FIG. 6. Comparison of WRF output and output from temperature retrievals, including different time tendency terms for 0000 UTC 20 Sep 2005 at (a) 4 and (b) 8 km altitude. The parameter  $\theta'_p$  (shaded, K) is shown for (from left to right) WRF output, retrieval with 1-min time tendency term, retrieval with 20-min time tendency term, and retrieval without time tendency term.

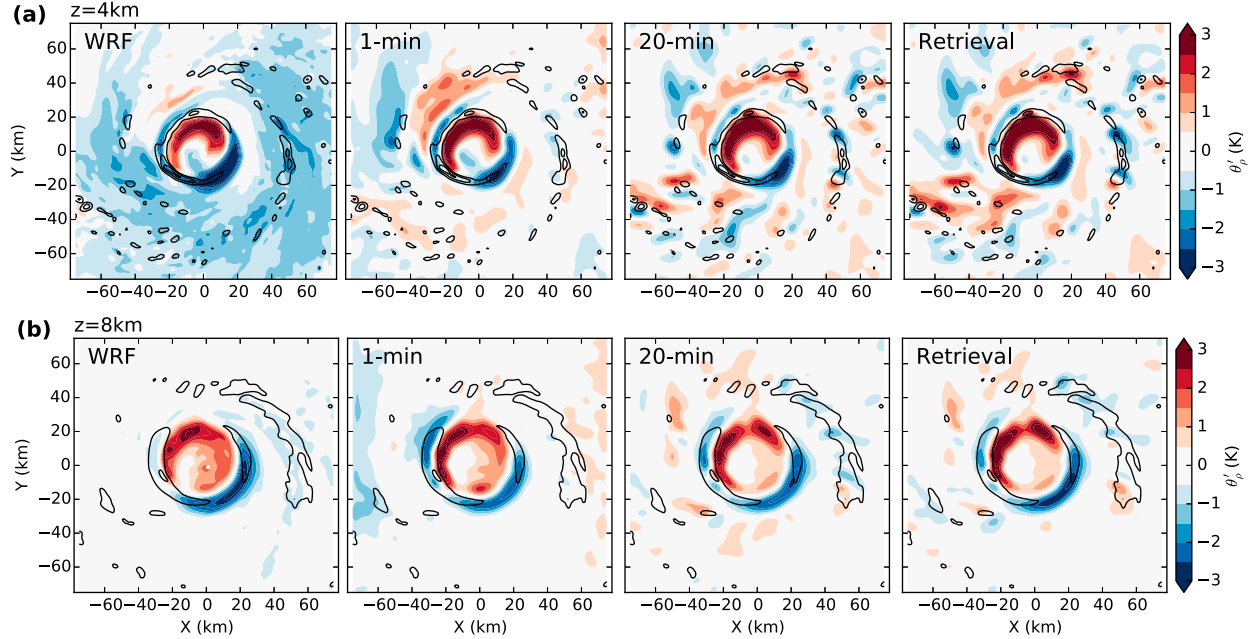


FIG. 7. Comparison of WRF output and output from temperature retrievals including different time tendency terms for 1800 UTC 21 Sep 2005 as in Fig. 6.

value averaged over all eight times is identical for the noise-free retrieval and  $1 \text{ m s}^{-1}$  noise retrieval, and only 0.02 higher for the  $2 \text{ m s}^{-1}$  noise retrieval. The % sign value is identical for noise-free retrieval and  $1 \text{ m s}^{-1}$  noise retrieval, and 1% lower for the  $2 \text{ m s}^{-1}$  noise retrieval. In other words, the statistics for normalized pressure perturbations and density potential temperature perturbations for the  $1 \text{ m s}^{-1}$  noise retrieval are identical to the averages for the noise-free retrieval, whereas the statistics for the  $2 \text{ m s}^{-1}$  noise retrieval are only marginally worse. The sensitivity of the retrieval to Gaussian noise depends on the filter settings of the retrieval. In this study we used a spline cutoff filter and a Gaussian filter to smooth the retrieval, hence making the retrieval less sensitive to noise.

One way to potentially remove noise in the retrieval is to smooth the input field. The sensitivity of the retrieval to the input resolution was tested by smoothing the WRF input fields by increasing the spline filter length from 4 to 10 grid points in step 1 of the retrieval (e.g., the multi-Doppler wind retrieval when using real data). The results of this test (not shown) do improve the verification with higher SCC, higher sign percentage, and lower RMSE, but they also reduce the maximum and RMS values of both the simulated and retrieved thermodynamic fields. The mesoscale thermodynamic structure is largely unaffected, but the details of small-scale features change in both the simulated and retrieved fields. Additional details of this test can be found in Foerster (2016) for interested

readers. Since the spatial resolution, resolved scales, and accuracy of both the wind and thermodynamic retrievals depend strongly on the Doppler velocity quality and sampling, it is not possible to recommend a specific filter length for all cases. Given the reasonably good accuracy of the retrieval in the presence of noise, we apply the retrieval to real data in the next section with the four gridpoint filter lengths to retrieve a higher level of detail. The highest confidence is in both the structure and magnitude of larger, stronger mesoscale perturbations rather than the smaller, weaker perturbations. As with

TABLE 3. Statistics for the evaluation of the *bias-corrected* pressure retrieval against the WRF output in terms of  $\langle p' \rangle$  (hPa) for eight different times (0000 UTC 20 Sep 2005–1800 UTC 21 Sep 2005): average pressure perturbation for retrieval ( $\langle p' \rangle$  TR) and WRF output ( $\langle p' \rangle$  WRF), RMS of  $p'$  for the bias-corrected retrieval (RMS TR), RMSE of bias-corrected  $p'$  (RMSE), SCC for the bias-corrected  $p'$ , and the bias-corrected percentage of grid points with the correctly retrieved sign (% sign).

Time and date	$\langle p' \rangle$ TR	$\langle p' \rangle$ WRF	RMS TR	RMS RMSE	SCC $p'$	% sign
0000 UTC 20 Sep	0.00	0.01	0.18	0.18	0.64	92
0600 UTC 20 Sep	0.02	-0.01	0.16	0.16	0.68	94
1200 UTC 20 Sep	0.02	-0.09	0.28	0.15	0.87	96
1800 UTC 20 Sep	0.02	0.14	0.26	0.15	0.80	94
0000 UTC 21 Sep	0.01	0.06	0.22	0.15	0.78	93
0600 UTC 21 Sep	0.03	0.11	0.37	0.22	0.89	93
1200 UTC 21 Sep	0.01	-0.04	0.67	0.29	0.94	88
1800 UTC 21 Sep	0.01	0.17	0.69	0.27	0.95	94

TABLE 4. Statistics for the evaluation of the bias-corrected temperature retrieval against the WRF output in terms of  $\theta'_p$  (K) for eight different times (0000 UTC 20 Sep 2005–1800 UTC 21 Sep 2005): average temperature perturbation for retrieval ( $\langle \theta'_p \rangle$  TR) and WRF output ( $\langle \theta'_p \rangle$  WRF), RMS of  $\theta'_p$  for the bias-corrected retrieval (RMS TR), RMSE of bias-corrected  $\theta'_p$  (RMSE), SCC for the bias-corrected  $\theta'_p$ , and the bias-corrected percentage of grid points with the correctly retrieved sign (% sign).

Time and date	$\langle \theta'_p \rangle$ TR	$\langle \theta'_p \rangle$ WRF	RMS TR	RMS RMSE	SCC $\theta'_p$	% sign
0000 UTC 20 Sep	-0.02	-0.19	0.52	0.50	0.63	88
0600 UTC 20 Sep	-0.02	-0.00	0.55	0.60	0.64	84
1200 UTC 20 Sep	-0.01	-0.06	0.51	0.50	0.61	81
1800 UTC 20 Sep	0.00	-0.21	0.55	0.51	0.54	88
0000 UTC 21 Sep	-0.01	0.07	0.63	0.59	0.62	85
0600 UTC 21 Sep	0.01	-0.00	0.64	0.62	0.60	79
1200 UTC 21 Sep	0.01	-0.02	0.79	0.67	0.69	79
1800 UTC 21 Sep	0.01	-0.32	0.86	0.66	0.68	87

any data analysis, there is an inherent trade-off between the level of detail and accuracy that must be assessed on a case-by-case basis and interpreted appropriately when making scientific conclusions.

#### 4. Application to real data

This section will demonstrate the applicability of SAMURAI-TR using real data from Hurricane Rita

(2005) collected during the RAINEX field campaign. Retrieving temperature and pressure perturbations from real data adds more challenges. In most cases, the data coverage is not complete, and some regions will be out of the range of the radar, while other regions will not contain enough precipitation scatterers to return a usable signal. Moreover, the Cartesian wind components are not measured directly; they are derived from Doppler velocities from different viewing angles. Thus, the quality of the wind field depends on the scanning geometry and Doppler velocity quality.

RAINEX was the first experiment to use the high-resolution radar ELDORA in tropical cyclones and the first experiment to simultaneously use three airborne dual-Doppler radars (NRL P-3, N42, N43). Hence, it provides excellent data to test SAMURAI-TR. One of the days where Hurricane Rita was observed simultaneously by three aircraft was 23 September 2005, the day before it made landfall and was impacted by increased vertical wind shear. The data used to test the thermodynamic retrieval were collected within a period of 30 min, from 2130 to 2200 UTC. The flight tracks of NRL P-3, N42, and N43 are overlaid in Fig. 9. Data were first edited using an automatic editing script (Bell et al. 2013) and afterward edited manually to resolve unfolding issues and to remove sidelobes, second-trip echoes, and ground clutter that were not removed in the first step.

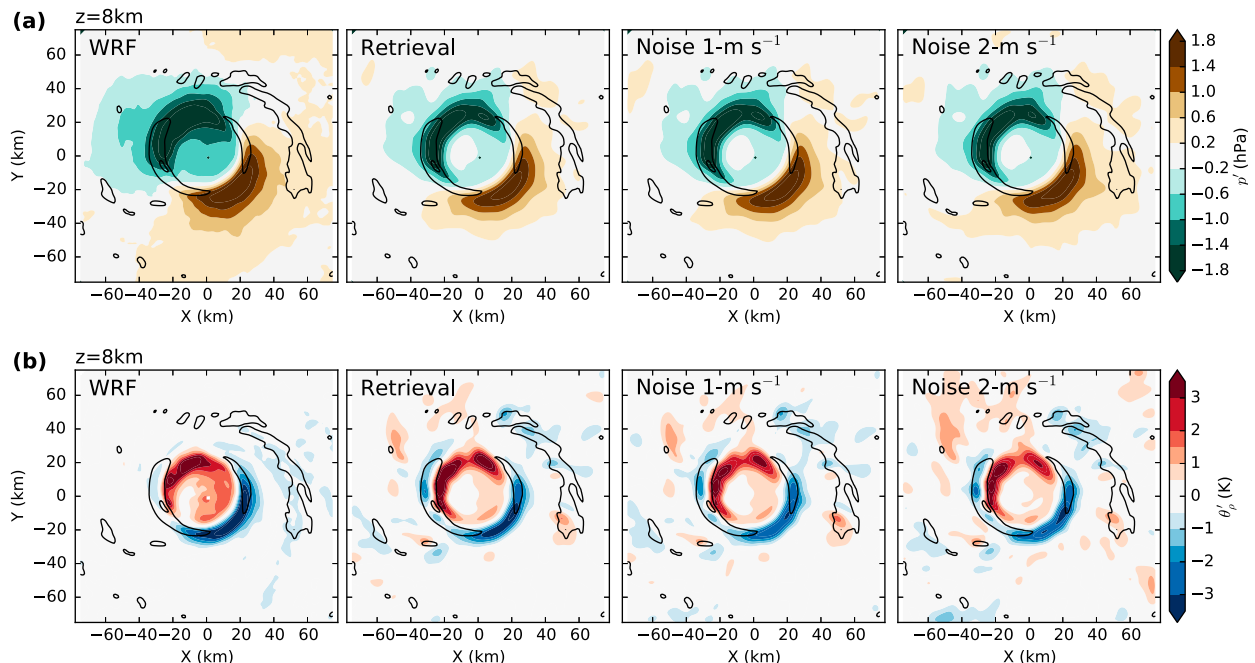


FIG. 8. Comparison of (from left to right) WRF output, retrieval without added noise, retrieval with Gaussian noise of  $1 \text{ m s}^{-1}$  standard deviation, and retrieval with Gaussian noise of  $2 \text{ m s}^{-1}$  standard deviation for 1800 UTC 21 Sep 2005 at 8 km altitude for (a)  $p'$  (shaded, hPa) and (b)  $\theta'_p$  (shaded, K).

### a. Wind retrieval

As outlined in the methodology section, the first step of the method is to combine the radar data and the complementary in-situ-flight-track, dropsonde, and atmospheric-motion-vector observations into a gridded SAMURAI analysis. A domain size of  $120 \text{ km} \times 120 \text{ km} \times 15 \text{ km}$  was used, with a horizontal resolution of 1 km and a vertical resolution of 0.5 km. The SAMURAI wind analysis was performed in two iterations, using a coarser spatial filter length in the first iteration and a finer filter in the second iteration to get a smooth analysis with an appropriate level of detail. This two-iteration approach is similar to that used in Barnes's (1964) objective analysis. A hybrid variational setting was used to derive the vertical velocity (Foerster et al. 2014), limiting the elevation angle to  $45^\circ$  and neglecting the projection of the terminal fall speed and the vertical wind component in the Doppler velocity, similar to the approach in a classical multi-Doppler synthesis but without the explicit integration of the mass continuity equation.

Horizontal cross sections of the "hexa-Doppler" SAMURAI analysis show a cyclonic wind field with an asymmetry in both the precipitation and the vertical velocity, illustrating the impact of the vertical wind shear on the storm's structure (Fig. 9). The highest radar reflectivity and the highest positive vertical velocities are found in the northeastern portion of the eyewall. The vertical velocity increases with height, while the reflectivity is strongest at low levels downwind of the updraft. The weakest reflectivity and strongest downdrafts are found in the southern and southwestern portions of the eyewall. The asymmetric convective structure is similar to that seen in other vertically sheared storms (Reasor and Eastin 2012; Foerster et al. 2014). The radar coverage is generally very good, with the entire eyewall being captured. However, there are gaps in the coverage at larger radii toward the northeast and especially toward the south and southwest, and in the eye. The size of the gaps increases with altitude as a result of decreasing scatterers.

### b. Balanced vortex retrieval

The second step of the method is to calculate the reference state for the pressure and temperature retrievals from the azimuthally averaged wind field and from vertical temperature and pressure profiles at the edge of the domain. The center of the storm at each vertical level is determined by finding the maximum mean vorticity, similar to the method of Marks et al. (1992). The mean center of the storm is defined as the average of the centers between 2 and 8 km altitude. This center is used to calculate the mean tangential wind field (Fig. 10a). The temperature and pressure profiles

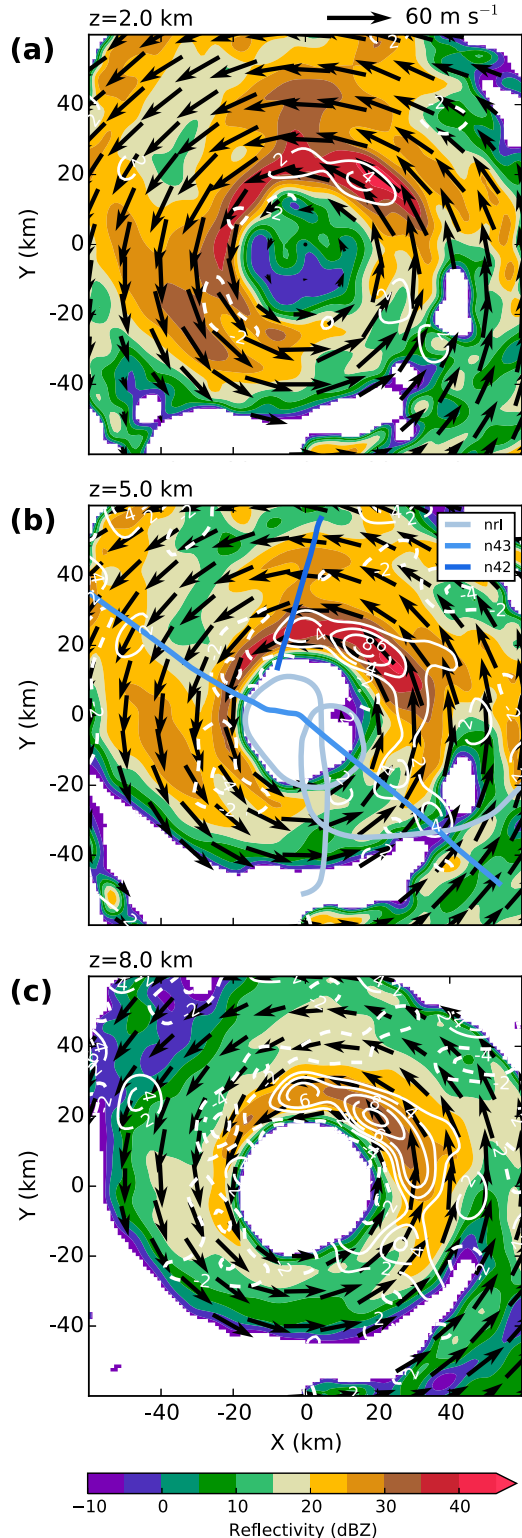


FIG. 9. SAMURAI analysis for 2130–2200 UTC 23 Sep 2005. Horizontal cross sections of radar reflectivity (shaded, dBZ), horizontal wind speed (wind vectors), and vertical wind speed (white contours,  $\text{m s}^{-1}$ ) at (a) 2, (b) 5, and (c) 8 km. Flight tracks of NRL P-3, N42, and N43 are overlaid in (b).

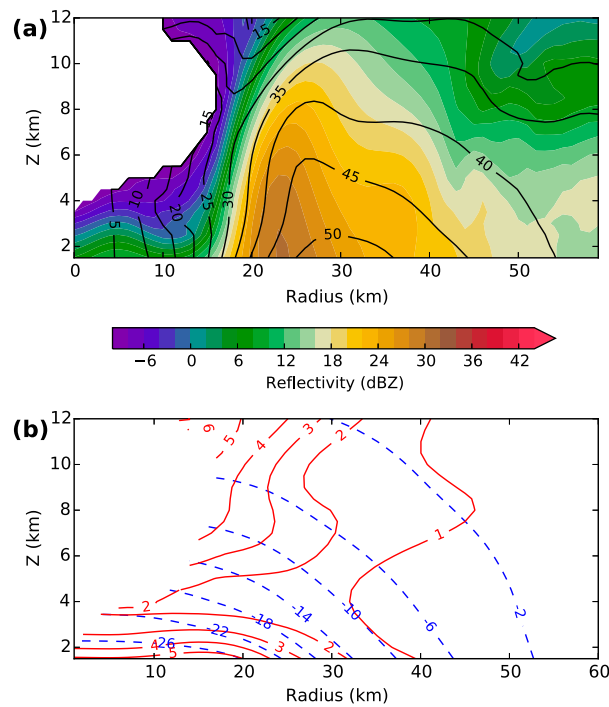


FIG. 10. SAMURAI analysis for 2130–2200 UTC 23 Sep 2005. (a) Azimuthally averaged storm structure of radar reflectivity (shaded, dBZ) and tangential wind speed (black contours,  $\text{m s}^{-1}$ ) for 0–60-km radius. (b) Mean pressure deficit (blue dashed, hPa) and temperature increase (red solid, K) relative to the mean pressure and temperature at a radius of 60 km at each respective vertical level, calculated from the mean tangential wind field in (a).

used to anchor the balanced vortex calculation are derived from the azimuthally averaged SAMURAI temperature and pressure field at a radius of 60 km. The inward integration of the thermal wind equation (Smith 2006) then allows for determining the mean temperature and pressure fields that balance the mean tangential wind field.

A pronounced temperature increase and a pronounced pressure drop toward the center are evident (Fig. 10b). The gaps in data coverage are either small enough or located favorably to not significantly affect the reference-state calculation. The coverage out to 60-km radius is good enough to calculate an azimuthally averaged tangential wind speed, although a slight bias might be introduced because the data gaps are located predominantly toward the south. The data gap in the eye of Hurricane Rita at levels above 4 km means that no reference pressure and temperature can be calculated there. Fortunately, the thermal wind equation is integrated inward and not outward, so the data gap in the eye does not affect other regions. In contrast, a data gap at larger radii would preclude the computation of the mean temperature and pressure everywhere inward of that radius.

### c. Thermodynamic retrieval

The third and final step of the method is the retrieval of the pressure and temperature perturbations with SAMURAI-TR. Similar to the radar reflectivity, the perturbations show a wavenumber-1 pattern at all heights (Fig. 11), which is consistent with the response of a vortex to vertical wind shear (Jones 1995). The regions of active convection toward the north and northwest of the center are characterized by positive pressure perturbations and negative temperature perturbations at low to midlevels (2–5 km; Figs. 11a,b,d,e). The pressure perturbations at upper levels (8 km; Figs. 11c,f) show negative pressure perturbations in the eastern portion of the eyewall, collocated with the deepest convection.

Apart from the broad-scale wavenumber-1 pattern, the pressure and temperature perturbations also show some smaller-scale features. A vertical cross section from the center toward the east (Fig. 12) shows positive pressure perturbations at low levels and small radii and negative pressure perturbations at upper levels and larger radii, which means that the pressure gradient force is directed upward and outward. The temperature perturbations are predominantly negative at low levels, with the exception of a region stretching from just outside the radius of maximum winds at around 25-km radius at 6-km height upward and outward. This pattern indicates raised isentropes at low levels, consistent with adiabatic ascent in this region, modulated by latent heat release within the eyewall convection, especially above the freezing level. An in-depth analysis of the radar-derived thermodynamic structure of Hurricane Rita and its relationship to vertical shear is beyond the scope of the current study and will be presented in a subsequent paper.

## 5. Summary and discussion

This study presents a thermodynamic retrieval tailored specifically toward rapidly rotating vortices that provides estimates of the pressure and temperature fields within the inner-core region of tropical cyclones using airborne Doppler radar data. Given the lack of our ability to fully sample the three-dimensional thermodynamic structure within rapidly rotating vortices directly, this new retrieval technique can provide insight into the physical mechanisms that are responsible for vortex intensification and structure change. The retrieval was evaluated using a WRF simulation of Hurricane Rita, and its applicability to real radar data was demonstrated.

The thermodynamic retrieval introduced here builds upon previous studies that use the momentum equations to derive temperature and pressure from a multi-Doppler

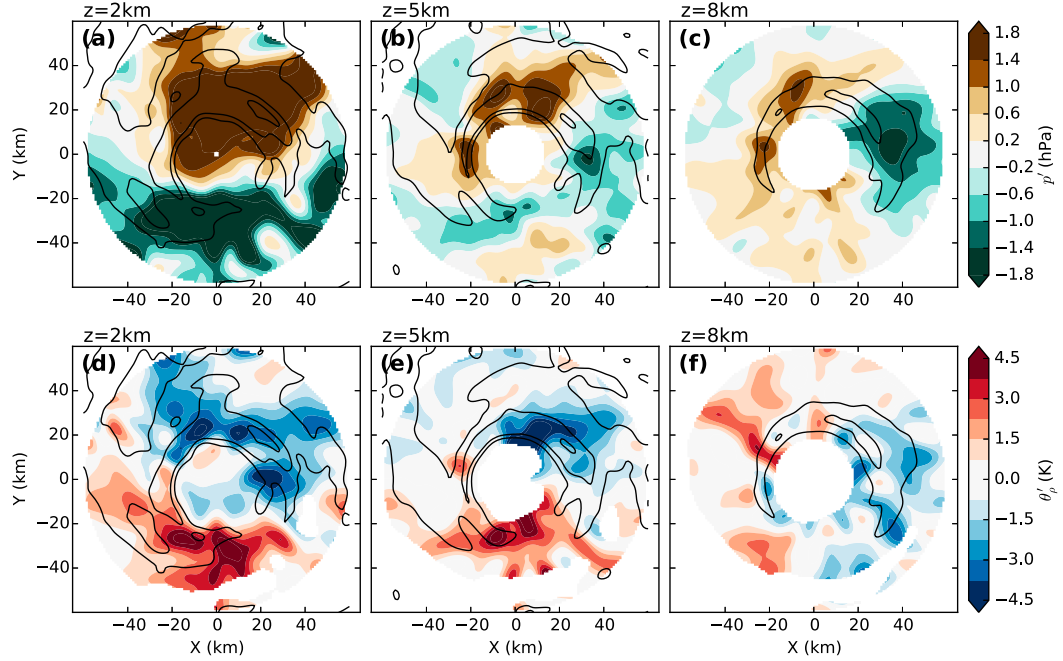


FIG. 11. Horizontal cross sections of (a)  $p'$  (shaded, hPa) and (b)  $\theta'_p$  (shaded, K) retrieved from the SAMURAI analysis in Fig. 9 for 2, 5, and 8 km altitude. Contours of radar reflectivity (20, 30, and 40 dBZ) are included for easier comparison. Grid points without wind field information or an undefined reference state (eye, outside of 60-km radius) are masked (white).

wind field. Similar to previous approaches, we use a variational formula to solve for the thermodynamic perturbations to an assumed reference state. The new technique presented here, coined “SAMURAI-TR,” advances the retrieval methodology in two key ways: 1) a reformulation of the retrieval equations to allow for horizontal variation in the reference state and 2) the use of a finite-element approach in the numerical formulation of the variational solver.

The first advance allows for a more appropriate reference state that changes with radius and height, and takes into account the steep mean gradients in pressure and temperature associated with strong vortices. The thermodynamic retrieval was designed primarily for tropical cyclones, but the direct applicability to other rapidly rotating vortices, such as tornados, is straight forward, and it can be easily adapted to a variety of scenarios. In the general formulation, any horizontally varying or homogeneous reference state could be used in the retrieval, potentially expanding the use of the technique beyond vortices. SAMURAI-TR could easily be used with a hydrostatic reference state for supercells or squall lines, or perhaps in a baroclinic environment where a horizontally varying reference-state definition is more suitable. For the current application, the azimuthal mean vortex in thermal wind balance was selected as the reference state because of the physical insight it provides for interpreting

the retrieved thermodynamic perturbations and the strong constraint it places on the magnitude of the horizontally averaged perturbations. The use of a horizontally varying balanced reference state provides the advantage of removing the need for an in situ vertical profile within the retrieval domain to resolve unknown integration constants. The vertical profile can instead be specified at the outer edge of the domain as an environmental reference, and small, unresolved horizontal averages of the perturbations can be neglected with only a slight degradation in the retrieval accuracy.

The second advance of this retrieval is a new technical implementation that differs from previous methods. Similar to the approach taken in SAMURAI, the retrieval minimizes a cost function using a Galerkin approach, with cubic B-spline finite elements as a basis. This allows one to directly specify gradients as pseudo-observations in the cost function, which is used to solve the classical problem of connecting the retrieval across vertical levels effectively. The implicit integration of the indirectly observed thermodynamic gradients provides a global solution that does not require the addition of the thermodynamic equation or a microphysical closure.

SAMURAI-TR has very good accuracy that is slightly better for pressure than for temperature, with root-mean-square errors of 0.25 hPa and 0.7 K, respectively. As a result of the retrieval design, the retrieval accuracy is

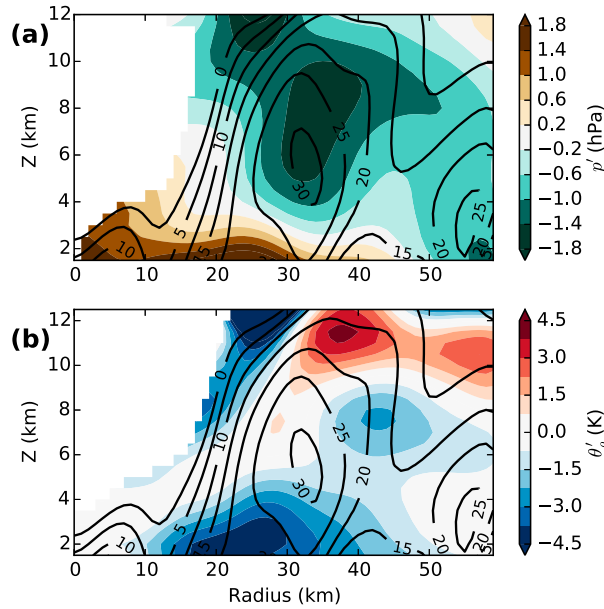


FIG. 12. Center-to-east cross sections of (a)  $p'$  (shaded, hPa) and (b)  $\theta'_p$  (shaded, K) retrieved from the SAMURAI analysis in Fig. 9, with radar reflectivity in black contours (dBZ). Grid points without wind field information or an undefined reference state are masked (white).

relatively insensitive to reasonable amounts of random noise. The accuracy is best in regions with high velocity gradients, such as the eyewall, and lower in regions with weak velocity gradients. While the inclusion of the time tendency terms in the retrieval equations would be desirable, it is not possible to compute them from airborne Doppler radar data at a meaningful time scale. Fortunately, sensitivity tests show that omitting the tendency terms only marginally affects the quality of the retrieval performance.

Spatial filter constraints are applied during the cost function minimization as essentially a background error covariance operator, which constrains the resulting three-dimensional spline function and mitigates the impact of small-scale variations in the wind field and noise. As with any retrieval, there is an inherent trade-off in the amount of smoothing and noise, such that increasing the filter length scales can reduce the mean error at the expense of some detail. Careful selection and interpretation of the resolved spatial scales is recommended when applying the technique.

The formulation of the cost function allows for straightforward incorporation of in situ thermodynamic measurements obtained by aircraft, dropsondes, or other measurements into the analysis. In addition to the direct constraint on the solution at the in situ locations, thermodynamic measurements could be used to estimate any unresolved horizontal averages of the perturbations. However, since in situ measurements are

made on different space and time scales than the radar volume, some care needs to be taken to properly specify the representativeness error if these additional observations were included. Likewise, direct comparison of the retrieved thermodynamics and in situ measurements is somewhat like comparing radar-estimated rainfall and rain gauge accumulation. While the latter can be considered “ground truth,” the mismatch in spatial and temporal resolution requires careful consideration when used for validation. Future improvements to the technique will investigate the optimal ways to use in situ observations in the retrieval and further validate the accuracy with real data.

One limitation of this study is that the retrieval solves for density potential temperature, and not separately for temperature, humidity, and water loading. Using density potential temperature is an advantage because of the simplicity of the retrieval equations, but it complicates the interpretation of the results, since the retrieved buoyancy can result from different combinations of thermal, water-vapor, liquid, and ice contributions. Radar reflectivity or polarimetric variables could be used to estimate the amount of water loading but disentangling the respective contributions of temperature and water vapor would not be possible without further assumptions about saturation or some additional measurements, such as a microwave radiometer. However, even without further decomposition, the three-dimensional density potential temperature field still can provide insight into convective forcing. SAMURAI-TR will be used in a follow-on study to analyze the effects of buoyancy and perturbation pressure gradients on the vertical motion with the goal of improving our understanding of the convective forcing mechanisms in the TC eyewall.

**Acknowledgments.** We are thankful for the valuable comments and suggestions of Gary Barnes, Jennifer Griswold, Patrick Harr, Albert Kim, Wen-Chau Lee, Alain Protat, and an anonymous reviewer. We acknowledge the RAINEX field campaign for collecting the data used in this manuscript. The research was supported by the National Science Foundation under Award AGS-1349881 and the Office of Naval Research under Award N000141410118.

## REFERENCES

- Barnes, S. L., 1964: A technique for maximizing details in numerical weather map analysis. *J. Appl. Meteor.*, **3**, 396–409, doi:[10.1175/1520-0450\(1964\)003<0396:ATFMDI>2.0.CO;2](https://doi.org/10.1175/1520-0450(1964)003<0396:ATFMDI>2.0.CO;2).
- Bell, M. M., M. T. Montgomery, and K. A. Emanuel, 2012: Air-sea enthalpy and momentum exchange at major hurricane wind speeds observed during CBLAST. *J. Atmos. Sci.*, **69**, 3197–3222, doi:[10.1175/JAS-D-11-0276.1](https://doi.org/10.1175/JAS-D-11-0276.1).

- , W.-C. Lee, C. A. Wolff, and H. Cai, 2013: A solo-based automated quality control algorithm for airborne tail Doppler radar data. *J. Appl. Meteor. Climatol.*, **52**, 2509–2528, doi:[10.1175/JAMC-D-12-0283.1](https://doi.org/10.1175/JAMC-D-12-0283.1).
- Braun, S. A., 2002: A cloud-resolving simulation of Hurricane Bob (1991): Storm structure and eyewall buoyancy. *Mon. Wea. Rev.*, **130**, 1573–1592, doi:[10.1175/1520-0493\(2002\)130<1573:ACRSOH>2.0.CO;2](https://doi.org/10.1175/1520-0493(2002)130<1573:ACRSOH>2.0.CO;2).
- Davis, C., and Coauthors, 2008: Prediction of landfalling hurricanes with the Advanced Hurricane WRF Model. *Mon. Wea. Rev.*, **136**, 1990–2005, doi:[10.1175/2007MWR2085.1](https://doi.org/10.1175/2007MWR2085.1).
- Doswell, C. A., III, and P. M. Markowski, 2004: Is buoyancy a relative quantity? *Mon. Wea. Rev.*, **132**, 853–863, doi:[10.1175/1520-0493\(2004\)132<0853:IBARQ>2.0.CO;2](https://doi.org/10.1175/1520-0493(2004)132<0853:IBARQ>2.0.CO;2).
- Dudhia, J., 1989: Numerical study of convection observed during winter monsoon experiment using a mesoscale two-dimensional model. *J. Atmos. Sci.*, **46**, 3077–3107, doi:[10.1175/1520-0469\(1989\)046<3077:NSOCOD>2.0.CO;2](https://doi.org/10.1175/1520-0469(1989)046<3077:NSOCOD>2.0.CO;2).
- Dunion, J. P., 2011: Rewriting the climatology of the tropical North Atlantic and Caribbean Sea atmosphere. *J. Climate*, **24**, 893–908, doi:[10.1175/2010JCLI3496.1](https://doi.org/10.1175/2010JCLI3496.1).
- Eastin, M. D., W. M. Gray, and P. G. Black, 2005: Buoyancy of convective vertical motions in the inner core of intense hurricanes. Part I: General statistics. *Mon. Wea. Rev.*, **133**, 188–208, doi:[10.1175/MWR-2848.1](https://doi.org/10.1175/MWR-2848.1).
- Ek, M. B., K. E. Mitchell, Y. Lin, E. Rogers, P. Grunmann, V. Koren, G. Gayno, and J. D. Tarpley, 2003: Implementation of Noah land surface model advances in the National Centers for Environmental Prediction operational mesoscale Eta model. *J. Geophys. Res.*, **108**, 2156–2202, doi:[10.1029/2002JD003296](https://doi.org/10.1029/2002JD003296).
- Foerster, A. M., 2016: Radar-derived thermodynamic structure of a major hurricane in vertical wind shear. Ph.D. thesis, University of Hawai‘i at Mānoa, 116 pp.
- , M. M. Bell, P. A. Harr, and S. C. Jones, 2014: Observations of the eyewall structure of Typhoon Sinlaku (2008) during the transformation stage of extratropical transition. *Mon. Wea. Rev.*, **142**, 3372–3392, doi:[10.1175/MWR-D-13-00313.1](https://doi.org/10.1175/MWR-D-13-00313.1).
- Gal-Chen, T., 1978: A method for the initialization of the anelastic equations: Implications for matching models with observations. *Mon. Wea. Rev.*, **106**, 587–606, doi:[10.1175/1520-0493\(1978\)106<0587:AMFTIO>2.0.CO;2](https://doi.org/10.1175/1520-0493(1978)106<0587:AMFTIO>2.0.CO;2).
- Gao, J., M. Xue, K. Brewster, and K. K. Droege, 2004: A three-dimensional variational data analysis method with recursive filter for Doppler radars. *J. Atmos. Oceanic Technol.*, **21**, 457–469, doi:[10.1175/1520-0426\(2004\)021<0457:ATVDAM>2.0.CO;2](https://doi.org/10.1175/1520-0426(2004)021<0457:ATVDAM>2.0.CO;2).
- Guimond, S. R., M. A. Bourassa, and P. D. Reasor, 2011: A latent heat retrieval and its effects on the intensity and structure change of Hurricane Guillermo (1997). Part I: The algorithm and observations. *J. Atmos. Sci.*, **68**, 1549–1567, doi:[10.1175/2011JAS3700.1](https://doi.org/10.1175/2011JAS3700.1).
- Hildebrand, P. H., and Coauthors, 1996: The ELDORA/ASTRAIA airborne Doppler weather radar: High-resolution observations from TOGA COARE. *Bull. Amer. Meteor. Soc.*, **77**, 213–232, doi:[10.1175/1520-0477\(1996\)077<0213:TEADWR>2.0.CO;2](https://doi.org/10.1175/1520-0477(1996)077<0213:TEADWR>2.0.CO;2).
- Hong, S.-Y., Y. Noh, and J. Dudhia, 2006: A new vertical diffusion package with an explicit treatment of entrainment processes. *Mon. Wea. Rev.*, **134**, 2318–2341, doi:[10.1175/MWR3199.1](https://doi.org/10.1175/MWR3199.1).
- Houze, R. A., Jr., and Coauthors, 2006: The hurricane rainband and intensity change experiment: Observations and modeling of Hurricanes Katrina, Ophelia, and Rita. *Bull. Amer. Meteor. Soc.*, **87**, 1503–1521, doi:[10.1175/BAMS-87-11-1503](https://doi.org/10.1175/BAMS-87-11-1503).
- Jones, S. C., 1995: The evolution of vortices in vertical shear. I: Initially barotropic vortices. *Quart. J. Roy. Meteor. Soc.*, **121**, 821–851, doi:[10.1002/qj.49712152406](https://doi.org/10.1002/qj.49712152406).
- Kain, J. S., and J. M. Fritsch, 1990: A one-dimensional entraining detrainning plume model and its application in convective parameterization. *J. Atmos. Sci.*, **47**, 2784–2802, doi:[10.1175/1520-0469\(1990\)047<2784:AODEPM>2.0.CO;2](https://doi.org/10.1175/1520-0469(1990)047<2784:AODEPM>2.0.CO;2).
- Lee, W.-C., and J. Wurman, 2005: Diagnosed three-dimensional axisymmetric structure of the Mulhall tornado on 3 May 1999. *J. Atmos. Sci.*, **62**, 2373–2393, doi:[10.1175/JAS3489.1](https://doi.org/10.1175/JAS3489.1).
- Lemaitre, Y., A. Protat, and G. Scialom, 1999: Dynamics of a bomb-like deepening secondary cyclone from airborne Doppler radar. *Quart. J. Roy. Meteor. Soc.*, **125**, 2797–2818, doi:[10.1256/smsqj.56001](https://doi.org/10.1256/smsqj.56001).
- Liou, Y.-C., 2001: The derivation of absolute potential temperature perturbations and pressure gradients from wind measurements in three-dimensional space. *J. Atmos. Oceanic Technol.*, **18**, 577–590, doi:[10.1175/1520-0426\(2001\)018<0577:TDOAPT>2.0.CO;2](https://doi.org/10.1175/1520-0426(2001)018<0577:TDOAPT>2.0.CO;2).
- , and Y.-J. Chang, 2009: A variational multiple Doppler radar three-dimensional wind synthesis method and its impacts on thermodynamic retrieval. *Mon. Wea. Rev.*, **137**, 3992–4010, doi:[10.1175/2009MWR2980.1](https://doi.org/10.1175/2009MWR2980.1).
- , T.-C. C. Wang, and K.-S. Chung, 2003: Three-dimensional variational approach for deriving the thermodynamic structure using Doppler wind observations—An application to a subtropical squall line. *J. Appl. Meteor.*, **42**, 1443–1454, doi:[10.1175/1520-0450\(2003\)042<1443:ATVAFD>2.0.CO;2](https://doi.org/10.1175/1520-0450(2003)042<1443:ATVAFD>2.0.CO;2).
- , J.-L. Chiou, W.-H. Chen, and H.-Y. Yu, 2014: Improving the model convective storm quantitative precipitation nowcasting by assimilating state variables retrieved from multiple-Doppler radar observations. *Mon. Wea. Rev.*, **142**, 4017–4035, doi:[10.1175/MWR-D-13-00315.1](https://doi.org/10.1175/MWR-D-13-00315.1).
- Marks, F. D., Jr., R. A. Houze Jr., and J. F. Gamache, 1992: Dual-aircraft investigation of the inner core of Hurricane Norbert. Part I: Kinematic structure. *J. Atmos. Sci.*, **49**, 919–942, doi:[10.1175/1520-0469\(1992\)049<0919:DAIOTI>2.0.CO;2](https://doi.org/10.1175/1520-0469(1992)049<0919:DAIOTI>2.0.CO;2).
- Marquis, J., Y. Richardson, P. Markowski, D. Dowell, J. Wurman, K. Kosiba, P. Robinson, and G. Romine, 2014: An investigation of the Goshen County, Wyoming, tornadic supercell of 5 June 2009 using EnKF assimilation of mobile mesonet and radar observations collected during VORTEX2. Part I: Experiment design and verification of the EnKF analyses. *Mon. Wea. Rev.*, **142**, 530–554, doi:[10.1175/MWR-D-13-00007.1](https://doi.org/10.1175/MWR-D-13-00007.1).
- Mlawer, E. J., S. J. Taubman, P. D. Brown, M. J. Iacono, and S. A. Clough, 1997: Radiative transfer for inhomogeneous atmospheres: RRTM, a validated correlated-k model for the longwave. *J. Geophys. Res.*, **102**, 16 663–16 682, doi:[10.1029/97JD00237](https://doi.org/10.1029/97JD00237).
- Ooyama, K. V., 1987: Scale-controlled objective analysis. *Mon. Wea. Rev.*, **115**, 2479–2506, doi:[10.1175/1520-0493\(1987\)115<2479:SCOA>2.0.CO;2](https://doi.org/10.1175/1520-0493(1987)115<2479:SCOA>2.0.CO;2).
- , 2002: The cubic-spline transform method: Basic definitions and tests in a 1D single domain. *Mon. Wea. Rev.*, **130**, 2392–2415, doi:[10.1175/1520-0493\(2002\)130<2392:TCSTMB>2.0.CO;2](https://doi.org/10.1175/1520-0493(2002)130<2392:TCSTMB>2.0.CO;2).
- Protat, A., and I. Zawadzki, 2000: Optimization of dynamic retrievals from a multiple-Doppler radar network. *J. Atmos. Oceanic Technol.*, **17**, 753–760, doi:[10.1175/1520-0426\(2000\)017<0753:OODRFA>2.0.CO;2](https://doi.org/10.1175/1520-0426(2000)017<0753:OODRFA>2.0.CO;2).
- , and Y. Lemaitre, 2001: Scale interactions involved in the initiation, structure, and evolution of the 15 December 1992 MCS observed during TOGA COARE. Part II: Mesoscale and convective-scale processes. *Mon. Wea. Rev.*, **129**, 1779–1808, doi:[10.1175/1520-0493\(2001\)129<1779:SIHTI>2.0.CO;2](https://doi.org/10.1175/1520-0493(2001)129<1779:SIHTI>2.0.CO;2).
- , —, and G. Scialom, 1998: Thermodynamic analytic fields from Doppler-radar data by means of the MANDOP analysis. *Quart. J. Roy. Meteor. Soc.*, **124**, 1633–1668, doi:[10.1002/qj.49712454914](https://doi.org/10.1002/qj.49712454914).

- Purser, R. J., W.-S. Wu, D. F. Parrish, and N. M. Roberts, 2003: Numerical aspects of the application of recursive filters to variational statistical analysis. Part I: Spatially homogeneous and isotropic Gaussian covariances. *Mon. Wea. Rev.*, **131**, 1524–1535, doi:[10.1175/1520-0493\(2003\)131<1524:NAOTAO>2.0.CO;2](https://doi.org/10.1175/1520-0493(2003)131<1524:NAOTAO>2.0.CO;2).
- Reasor, P. D., and M. D. Eastin, 2012: Rapidly intensifying Hurricane Guillermo (1997). Part II: Resilience in shear. *Mon. Wea. Rev.*, **140**, 425–444, doi:[10.1175/MWR-D-11-00080.1](https://doi.org/10.1175/MWR-D-11-00080.1).
- Roux, F., 1985: Retrieval of thermodynamic fields from multiple-Doppler radar data using the equations of motion and the thermodynamic equation. *Mon. Wea. Rev.*, **113**, 2142–2157, doi:[10.1175/1520-0493\(1985\)113<2142:ROTFFM>2.0.CO;2](https://doi.org/10.1175/1520-0493(1985)113<2142:ROTFFM>2.0.CO;2).
- , 1988: The West African squall line observed on 23 June 1981 during COPT 81: Kinematics and thermodynamics of the convective region. *J. Atmos. Sci.*, **45**, 406–426, doi:[10.1175/1520-0469\(1988\)045<0406:TWASLO>2.0.CO;2](https://doi.org/10.1175/1520-0469(1988)045<0406:TWASLO>2.0.CO;2).
- , and S. Ju, 1990: Single-Doppler observations of a West African squall line on 27–28 May 1981 during COPT 81: Kinematics, thermodynamics and water budget. *Mon. Wea. Rev.*, **118**, 1826–1854, doi:[10.1175/1520-0493\(1990\)118<1826:SDOOAW>2.0.CO;2](https://doi.org/10.1175/1520-0493(1990)118<1826:SDOOAW>2.0.CO;2).
- , V. Marecal, and D. Hauser, 1993: The 12/13 January 1988 narrow cold-frontal rainband observed during MFDP/FRONTs 87. Part I: Kinematics and thermodynamics. *J. Atmos. Sci.*, **50**, 951–974, doi:[10.1175/1520-0469\(1993\)050<0951:TJNCFR>2.0.CO;2](https://doi.org/10.1175/1520-0469(1993)050<0951:TJNCFR>2.0.CO;2).
- Smith, R. K., 2006: Accurate determination of a balanced axisymmetric vortex in a compressible atmosphere. *Tellus*, **58A**, 98–103, doi:[10.1111/j.1600-0870.2006.00149.x](https://doi.org/10.1111/j.1600-0870.2006.00149.x).
- , M. T. Montgomery, and H. Zhu, 2005: Buoyancy in tropical cyclones and other rapidly rotating atmospheric vortices. *Dyn. Atmos. Oceans*, **40**, 189–208, doi:[10.1016/j.dynatmoce.2005.03.003](https://doi.org/10.1016/j.dynatmoce.2005.03.003).
- Tai, S.-L., Y.-C. Liou, J. Sun, and S.-F. Chang, 2017: The development of a terrain-resolving scheme for the forward model and its adjoint in the four-dimensional Variational Doppler Radar Analysis System (VDRAS). *Mon. Wea. Rev.*, **145**, 289–306, doi:[10.1175/MWR-D-16-0092.1](https://doi.org/10.1175/MWR-D-16-0092.1).
- Thompson, G., and T. Eidhammer, 2014: A study of aerosol impacts on clouds and precipitation development in a large winter cyclone. *J. Atmos. Sci.*, **71**, 3636–3658, doi:[10.1175/JAS-D-13-0305.1](https://doi.org/10.1175/JAS-D-13-0305.1).
- Viltard, N., and F. Roux, 1998: Structure and evolution of Hurricane Claudette on 7 September 1991 from airborne Doppler radar observations. Part II: Thermodynamics. *Mon. Wea. Rev.*, **126**, 281–302, doi:[10.1175/1520-0493\(1998\)126<0281:SAEOHC>2.0.CO;2](https://doi.org/10.1175/1520-0493(1998)126<0281:SAEOHC>2.0.CO;2).
- Willoughby, H. E., 1990: Gradient balance in tropical cyclones. *J. Atmos. Sci.*, **47**, 265–274, doi:[10.1175/1520-0469\(1990\)047<0265:GBITC>2.0.CO;2](https://doi.org/10.1175/1520-0469(1990)047<0265:GBITC>2.0.CO;2).
- Zhang, D.-L., Y. Liu, and M. K. Yau, 2000: A multiscale numerical study of Hurricane Andrew (1992). Part III: Dynamically induced vertical motion. *Mon. Wea. Rev.*, **128**, 3772–3788, doi:[10.1175/1520-0493\(2001\)129<3772:AMNSOH>2.0.CO;2](https://doi.org/10.1175/1520-0493(2001)129<3772:AMNSOH>2.0.CO;2).